

NASA CR-173,300

DEPARTMENT OF AERONAUTICS & ASTRONAUTICS
MASSACHUSETTS INSTITUTE OF TECHNOLOGY
CAMBRIDGE, MASSACHUSETTS 02139

NASA-CR-173300
19840010018

FINAL REPORT ON NASA GRANT NSG-1-206

ENTITLED

A COOPERATIVE PROGRAM TO STIMULATE STUDENT INVOLVEMENT
THROUGH THE MIT UNDERGRADUATE RESEARCH
OPPORTUNITY PROGRAM

submitted to the

NASA LANGLEY RESEARCH CENTER
Hampton, Virginia 23665

Attn: Mr. John F. Royall, Jr.
Office of Research Grants and University Affairs
MS 105A

Dr. Robert A. Kilgore
MS 133

Principal
Investigators:

Eugene E. Covert
Earl M. Murman
Judson R. Baron
Wesley L. Harris, Sr.

Period of
Investigation:

September 1, 1982 - August 31, 1983

January 1984



NF01456

LIBRARY COPY

JUL 16 1984

LANGLEY RESEARCH CENTER
LIBRARY, NASA
HAMPTON, VIRGINIA

NASA CR-173,300

DEPARTMENT OF AERONAUTICS & ASTRONAUTICS
MASSACHUSETTS INSTITUTE OF TECHNOLOGY
CAMBRIDGE, MASSACHUSETTS 02139

FINAL REPORT ON NASA GRANT NSG-1-206

ENTITLED

A COOPERATIVE PROGRAM TO STIMULATE STUDENT INVOLVEMENT
THROUGH THE MIT UNDERGRADUATE RESEARCH
OPPORTUNITY PROGRAM

submitted to the

NASA LANGLEY RESEARCH CENTER
Hampton, Virginia 23665

Attn: Mr. John F. Royall, Jr.
Office of Research Grants and University Affairs
MS 105A

Dr. Robert A. Kilgore
MS 133

Principal
Investigators:

Eugene E. Covert
Earl M. Murman
Judson R. Baron
Wesley L. Harris, Sr.

Period of
Investigation:

September 1, 1982 - August 31, 1983

January 1984

LIBRARY COPY

JUL 16 1984

LANGLEY RESEARCH CENTER
LIBRARY, NASA
HAMPTON, VIRGINIA

INTRODUCTION

Under Grant NSG-1-206, members of the Faculty in the Department of Aeronautics and Astronautics at MIT, together with selected undergraduate students, have undertaken four projects as part of the Undergraduate Research Opportunities Program at MIT. The research under this grant is coordinated with specific Langley personnel, but not among the individual investigators. The remaining part of this report will consist of individual summaries by each of the four investigators. For convenience, the investigators are listed in alphabetical order.

N84-18086 #

PROGRESS REPORT: HOT WIRE IN LOW REYNOLDS NUMBER FLOW

Mark A. Kolb
Prof. E. E. Covert

Project Objective

The intent of this project is the study of the low Reynolds number flow phenomenon of periodic vortex shedding in the wake behind a cylinder, applying the hot wire anemometer technique of flow measurement. This work is concerned primarily with the downstream diffusion of these shed vortices. An evaluation of the performance of the hot wire at low Reynolds number will also be considered.

Progress to Date

This work began slowly last spring with the first faltering steps at becoming familiar with the facilities to be used at the MIT Gas Turbine Laboratory, where the work is being done. At this time, the concepts behind hot wire measurements, as presented in the literature, were also investigated.

Work in the summer began with the correlation of two sets of pressure measurements. The vortices are produced in a free jet (one-inch diameter) which flows from a tank connected to an oil-free compressor. Pitot tube measurements of the jet flow velocity were correlated with pressure tap measurements from the wall of the tank from which the jet flows. This enabled the hot wire calibration to be performed with respect to the pressure tap measurements, instead of against pitot tube measurements; simultaneous pitot tube and hot wire measurements might have been mutually inaccurate due to interference

effects inside the small jet.

Progress quickened mid-summer when the opportunity arose to begin constructing hot wire probes, and the work of constructing, calibrating, and repairing probes occupied most of the remainder of the summer. A sketch of the probe design is presented in Figure 1. Gold electrodes are soldered to a pair of broaches (round, dimensioned "0.0003" x 0.013"). The broaches are then inserted through a short length of ceramic tubing. The ends of the broaches, which protrude about half an inch from the tubing, are then bent in half to a 90° angle, 2.5 m-diameter platinum wire, Wollaston-drawn, with silver coating, is used for the "hot wire" itself. The silver coating is etched away from a few millimeters of wire, using nitric acid. This etched length is then soldered across the ends of the two broaches.

Present Work

Work has continued this fall using three of these hot wire probes. A DISA 55D01 Anemometer is employed to process the probe signals. A sketch of the present apparatus is shown in Figure 2.

The calibrated hot wires are being used to determine optimum conditions under which the wake vortices may be observed. Conditions such as flow speed and cylinder diameter have been varied while observing the output of the hot wire on an oscilloscope.

At first, several problems were encountered. Not considering the effects of the vortex's passage, sinusoidal output was originally sought. Figure 3, showing a typical wake velocity-time profile, indicates that, indeed, the flow is periodic - as expected - but it is

not sinusoidal. The passage of a vortex is indicated by the sudden bursts in output voltage. It appears that there may be an underlying sinusoidal signal (it is difficult to discern whether or not this is actually just an illusion created on the rapidly changing oscilloscope screen), but it is not likely that this is due to the vortex shedding. On the other hand, it does not appear in the trace of the free jet hot wire measurements (i.e., without the cylinder).

Originally, cylinders of too-small diameter were used, but the vortices were too difficult to locate. Present measurements (Figure 3 included) are for a 4.2 mm cylinder in the one-inch jet. Location of the cylinder in the jet (i.e., outside the zone of potential flow) was another hindrance to good results. A third problem concerns the flow velocity. To improve the vortex formation, flow speed was increased. The 0.96 V average output voltage in Figure 3 corresponds to a flow velocity on the order of 1.4 m/sec, for a Reynolds number based on cylinder diameter of about 380. This is well within the range for periodic vortex formation. If, however, the upstream speed is considered, a Reynolds number of almost 1800 is observed, which suggests a turbulent wake. Perhaps, then, the results presented in Figure 3 are not optimum.

Intentions

Upon establishing a working ability to distinguish the wake vortices, it is next desired to begin quantifying the wake parameters. The first measurements to be taken will concern the dimensions of the wake - in what region may the vortices be found? How far above and

below the cylinder? How far downstream? This can be accomplished simply by moving the hot wire probe and measuring the displacement with rulers. Preliminary results suggest that, at least for higher flow velocities, the edges of the wake are quite distinct.

The next quantity to be determined will be the speed of diffusion of the vortices downstream. Measurements of the frequency of the periodic hot wire signal at different locations in the wake will describe the velocity profile of the shed vortices. Another quantity to be measured might be the strength of the vortices, but a method for doing so has yet to be considered.

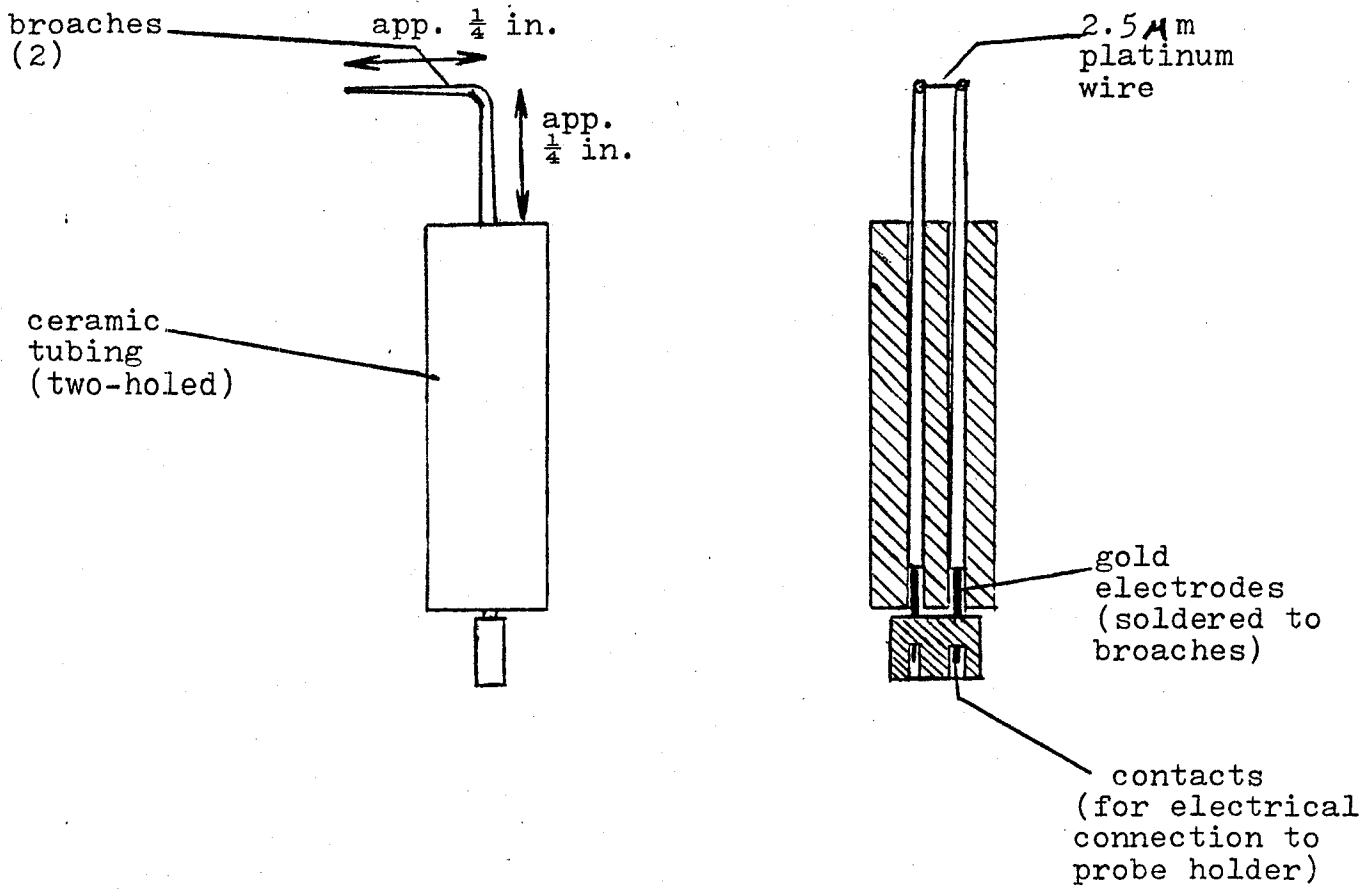


Figure 1. Sketch of hot wire probe design.

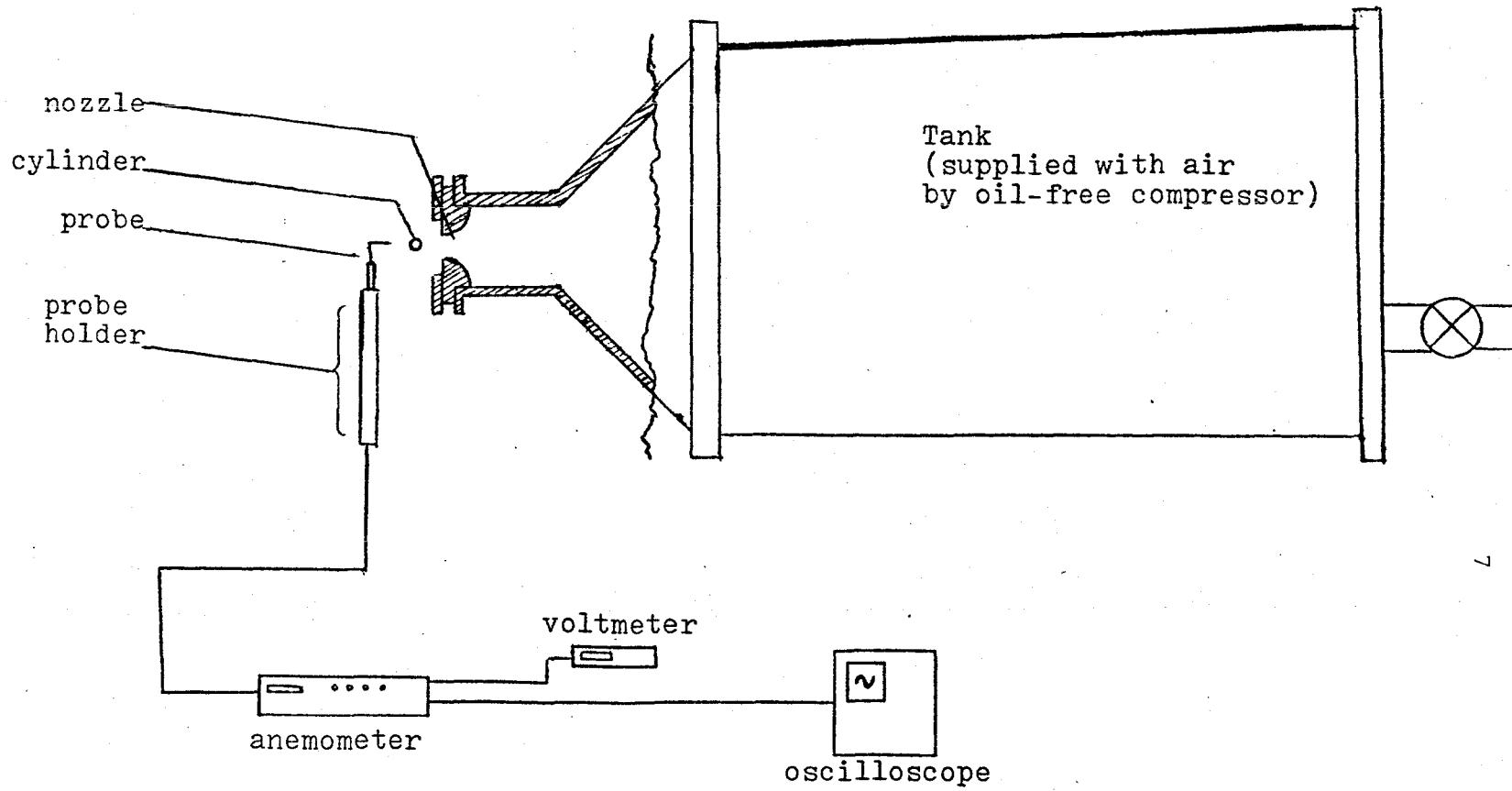


Figure 2. Sketch of present experimental set-up.

Flow Behavior in the Wright Brothers Facility

Investigators: Prof. Judson R. Baron
Mr. Stephen Genn

NASA Technical Monitor: Dr. Robert Kilgore

At various times during the last several years test results obtained in the Wright Brothers 7.5' x 10' wind tunnel have led to speculations as to the flowfield uniformity. Such test considerations are typical and always proper, and in combination with numerous alterations that have been made recently to the tunnel circuit did suggest that the flowfield should be reexamined.

The objective was seen to be twofold: 1) A brief examination of back sections of the circuit to establish whether or not gross flow deviations were present at corners, turning vane regions, etc., and 2) A calibration of the test section itself.

Both of these tasks were undertaken during the year and both the procedures and results of the project are described in the attached report (Flow Behavior in the Wright Brothers Facility, Stephen Genn, WBWT-TR-1187, September 1983). In essence rather substantial calibrations were obtained with total and static pressure instrumentation over large portions of two test section vertical planes, and five speeds in the range 35 to 125 mph (50 - 185 fps). The useful central core flow proves to extend over approximately 0.75 of horizontal and vertical spans of the elliptical test section, with dynamic pressure variations over the entire section being within 1%.

The report is attached as Appendix A.

Final Report on Development of Software for
Digital Signal Processing

Investigators: Professor W.L. Harris, V. Del Gaudio,
R. Edmonds, and S. Zachary

NASA Technical Monitor: Mr. D.R. Hoad, LSAD

The research efforts of this project were concentrated on the development of auto- and cross-covariance and of auto- and cross-correlation software. This Fortran code was written from a time and frequency domain analysis. A second development consisted of a code to compute the power spectrum. Both codes have been debugged and are available on IBM compatible 8" flexible disc.

Title of Task: Numerical Studies of Some Aspects of the 0.3 Meter
Cryogenic Self-Streamlining Wind Tunnel

Principal Investigator: Professor Earll M. Murman

Student: Jonathan Webb, Class of 1983

Final Summary of Progress:

This task involved developing a numerical simulation code to assess residual errors on airfoil loads due to imperfect shaping of the self-streamlining wall for the 0.3 meter cryogenic wind tunnel. Causes of imperfect shaping could result from pressure loadings on the wall and the finite number of jacks available to shape a wall representing a freestream streamline. It should be noted that previous development work for the wall included an estimate of such errors. However, the estimates had been made without using transonic computational methods. The current task involved writing a simple numerical model for the wall structure, modifying an existing transonic small disturbance code for the free air and self streamlining wall conditions, coupling the two codes together, and performing numerical simulations to quantify the residual errors.

A detailed summary on the progress of the research is contained in the attached report entitled "Adaptation of Two-Dimensional Transonic Analysis Code, TSFOIL, for Use in Modeling Adaptive Wall Test Sections" authored by the student (Appendix C). The structural code was written, the TSFOIL code modified, and the two codes hooked together. Unfortunately, by the time the student completed his undergraduate studies in May 1983, the calculations were not converging. It is not

known if there are errors in the formulation or the coding. This proved to be a rather challenging task to carry out within an undergraduate research project environment.

Title of Task: Induced Drag Predictions for Aircraft Configurations

Principal Investigator: Professor Earll M. Murman

Student: Richard Shapiro, Class of 1983

NASA Technical Monitor: Edward Waggoner

Final Summary of Progress:

This task was terminated shortly after it was initiated due to the unavailability of the student. No funds were expended on this task.

Title of Task: Calculating C-Grids with Fine and Embedded Mesh Regions

Principal Investigator: Professor Earll M. Murman

Student: Bernard Loyd, Class of 1983

NASA Technical Monitor: None

Final Summary of Progress:

This task was initiated during the summer of 1983 due to the availability of the student on rather short notice and the timeliness of the research topic. Research by a PhD student, Mr. William Usab, demonstrated the attractiveness of using embedded grids for airfoil calculations modeled by the Euler equations. Mr. Usab's work had been done exclusively using O-grids. It was desirable to extend these calculations to C-type grids both for Euler, and eventually, the Navier-Stokes calculations (see Appendix C).

During the summer of 1983, Mr. Loyd developed a C-grid generation code for an arbitrary airfoil shape. The method followed the Jameson-Caughey approach of a parabolic mapping followed by shearing and stretching transformations. A working and documented code was developed during the summer on a VAX 11/750, and in the fall Mr. Usab utilized the code for Euler and preliminary Navier-Stokes calculations. Comparison of the Euler results with the previous O-grid calculations demonstrated significant improvements in rates of convergence and required levels of artificial viscosity.

During the fall of 1983, Mr. Loyd extended the C-grid code to include the capability of embedding any number of refined grids within the solution domain. A detailed description of the work is included in

the attached report entitled "Calculating C-Grids with Fine and Embedded Mesh Regions" authored by the student. Mr. Loyd plans to continue working in this general area for his Masters thesis research.

Closing Remarks

In the last two years, eight undergraduates in the Department of Aeronautics and Astronautics were provided with opportunities to study problems of importance to several research tasks. The problems varied widely, from writing programs for computer aided experimentation to attempting to measure the decay rate of the vortices that make up the Karman vortex street. This latter issue is related to interpretation of certain flow visualization processes, i.e., does one have a long vortex street or just the marking points where the decayed vortex was?

In any case, the faculty feels the educational opportunity offered by this grant was great and that these students profitted greatly from their experience. As an experiment in a cooperative educational venture, we feel it was successful.

FLOW BEHAVIOR IN
THE WRIGHT BROTHERS FACILITY

Stephen Genn

WBWT-TR-1187

September 1983



**THE WRIGHT BROTHERS
MEMORIAL WIND TUNNEL - M.I.T.**

Department of Aeronautics and Astronautics

Cambridge, Massachusetts

FLOW BEHAVIOR IN
THE WRIGHT BROTHERS FACILITY.

Stephen Genn

WBWT-TR-1187

September 1983

Prepared with partial support of the
National Aeronautics and Space Administration
NASA Grant NSG-1-206
(MIT OSP 91161)

Wright Brothers Facility
Department of Aeronautics and Astronautics
Massachusetts Institute of Technology
Cambridge, Massachusetts 02139

TABLE OF CONTENTS

1. Introduction -----	1
2. Preliminary Observations, Back Leg, Section D -----	1
3. Calibration of Test Section, Model Station -----	5
3.1 Computer Output and Data -----	8
4. Calibration Data; TUNCAL.101-509 -----	9
5. Calibration of Test Section, Second Measurement Plane -----	9
6. Conclusion -----	10
APPENDIX I	
Data Reduction -----	11-13
APPENDIX II	
Photographs of Selected Rake Positions -----	14-15
APPENDIX III	
A. Uncorrected Calibration Data for TUNCAL.abc Files -----	16-18
B. Pressure Coefficient Distribution Across Tunnel Section -----	19-24
C. Contours of Constant Pressure Coefficient C_{p_n} -----	25-29
APPENDIX IV	
A. Uncorrected Calibration Data for TUNCA.2abc Files -----	30-31
B. Pressure Coefficient Distribution Across Tunnel Section -----	32-36
C. Contours of Constant Pressure Coefficient C_{p_n} -----	37-39

1. Introduction

It has become increasingly apparent that a reexamination of the flow characteristics in the low speed Wright Brothers Facility (WBF) is of some importance in view of recent improvements in the precision of the data acquisition system. In particular, the existence of local regions of separation, if any, in back portions of the circuit, and possible related unsteadiness, are of interest.

During April 1983 a preliminary qualitative experiment was performed to examine the nature of any problem. The test was performed in the upstream cross leg preceding the stilling section (marked Section D on Figure I-1). Observations from that initial experiment did indicate some unsteady air flow problems in the cross leg, and thereafter the test region (Section A) was calibrated quantitatively. The intent was to learn something about the effect of upstream intermittent behavior flow on the test section flow, as well as to provide an extensive calibration as a standard for the effects induced by future alteration of the tunnel.

Distributions of total pressure coefficients were measured first at one cross-section plane of the test section, namely the model station (Fig. I-1). Data were obtained for several tunnel speeds. The reduced data yielded an unexpected distribution involving larger pressures along the inside wall. It was conjectured, for example, that a rotation of the entire channel flow may exist. Consequently, a second calibration was performed in a plane located seven feet downstream of the model station.

The following sections describe the test conditions, procedures and results for the present unmodified tunnel circuit.

2. Preliminary Observations, Back Leg, Section D

On April 8, 1983, the initial observations were made in the Wright Brothers Facility in Section D (Fig. I-1). Although a grid pattern of tufts was conceived to aid in cataloguing observations, only the flow in the very central plane of Section D was observed (Fig. II-1).

The observed plane, however, was divided into a grid system as shown in Fig. II-2 .

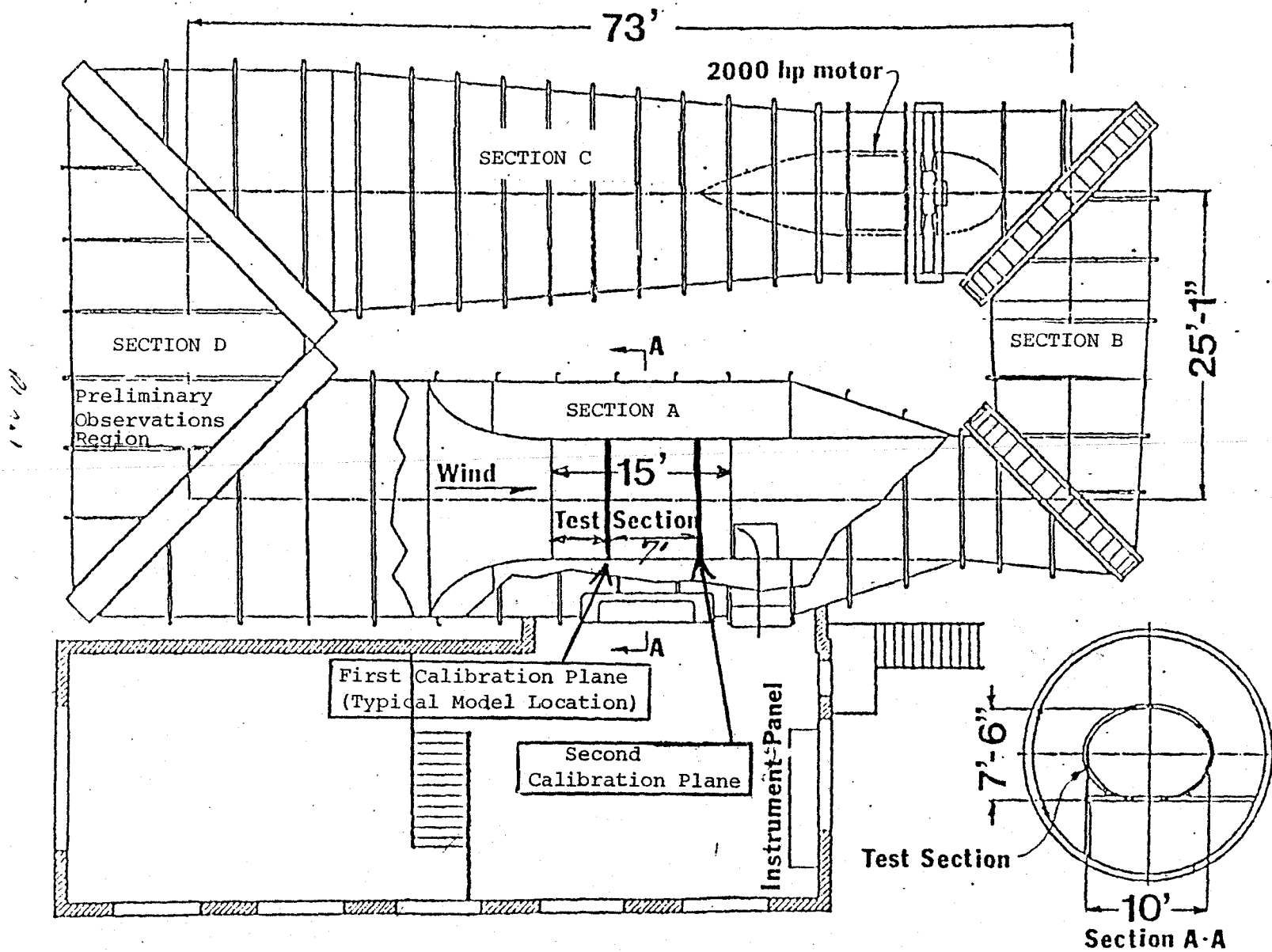


Fig. I-1. Plan view of Wright Brothers Facility with tested areas marked.

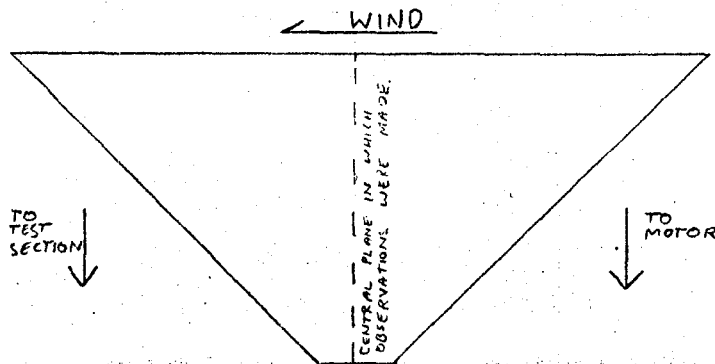


Fig. II-1. Plan view of Section D.

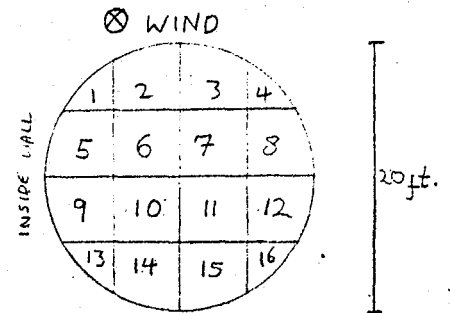


Fig. II-2. Cross-sectional view of grid at plane indicated in Fig. II-1.

A ten foot conduit pole with six two-foot yarn tufts spaced at six-inch intervals was used to observe the flow (Fig. II-3). All grid areas were within reach excepting #2 and #3 (Fig. II-2). The tunnel was run at a constant 40 mph (in test section) and photographs were taken to record phenomena of special interest.

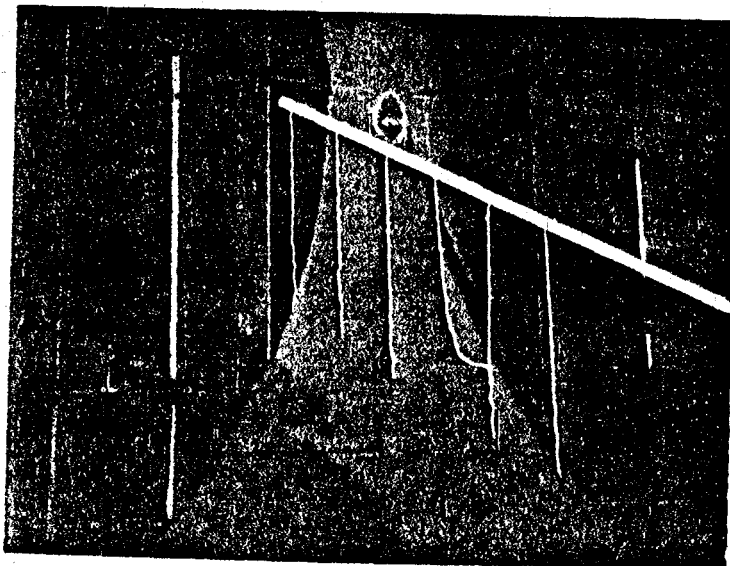


Fig. II-3. Photograph of tuft pole in Section D, looking towards inside wall.

OBSERVED:

Center region grid sections #6, 7, 10, 11:

All flow in these sections was observed to be steady.

Boundary grid sections #4, 8, 12, 16, 15, 14:

All flow, exclusive of a four to six inch boundary layer, was steady.

Inside wall grid sections 1, 5, 9, 13:

The flow did not appear to be turbulent in this region. However, there was a surging of sorts corresponding to a cyclical growth and decay of the flow velocity. The oscillatory velocity had no simple time dependence. The cycles were periods of the order of five to ten seconds (Figs. II-4 and II-5).

Fig. II-4. Double exposure showing the decaying flow phenomenon on the inside wall. Photo taken from grid section 11; view is of tufts on the border between sections 5 and 9.

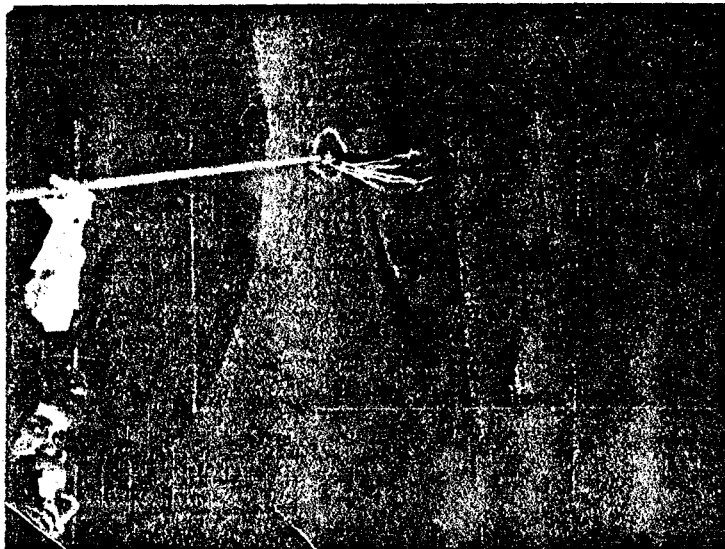
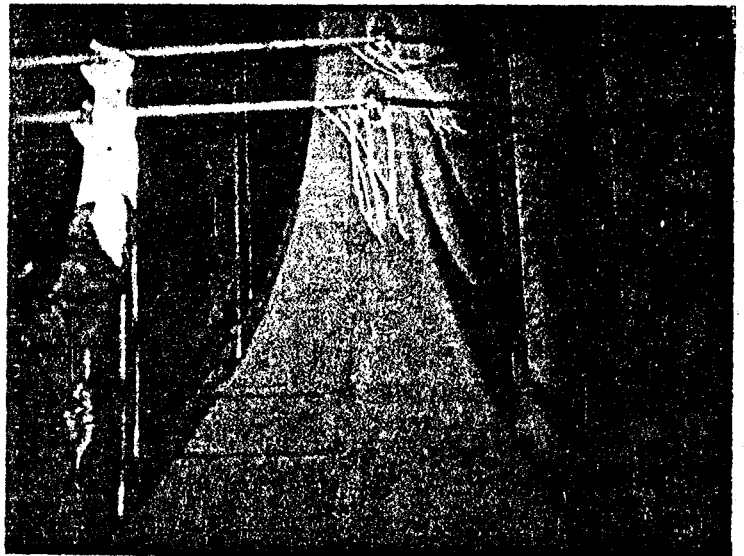


Fig. II-5. Tufts in normal steady flow of air. Photo taken five seconds after exposures shown in Fig. II-4.

3. Calibration of Test Section, Model Station

Total pressures were measured at the model station plane of the test section. Some static pressure measurements were also taken.

The tunnel was operated at five nominal velocities: 35, 50, 70, 100, and 125 mph. A device resembling a long rake with 21 pitot probes at four-inch intervals was moved through nine positions in one plane of the test section at the model station (Figs. III-1, III-5). Consequently, during this calibration there were $9 \times 5 = 45$ test runs.

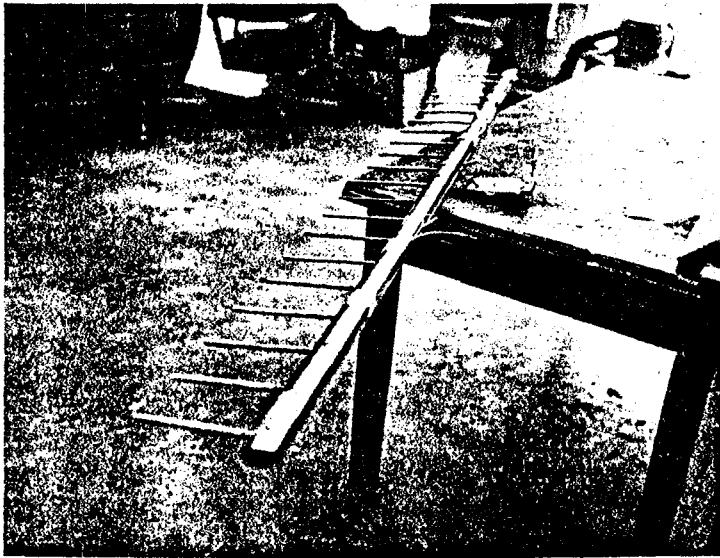


Fig. III-1. Total pressure rake.

In addition, the following were measured: total pressure at the upstream entrance to the test section, the average of four static pressures located at flush wall taps on and spaced evenly in a circumferential ring around the test section, and both total and static pressures at three pitot-static probes mounted in the test plane (Figs. III-2a and III-2b). The pressure at each such tap was measured during each test run.

The rake was held in place on two steel unistrut P-400 bars with C-clamps (Fig. III-3).

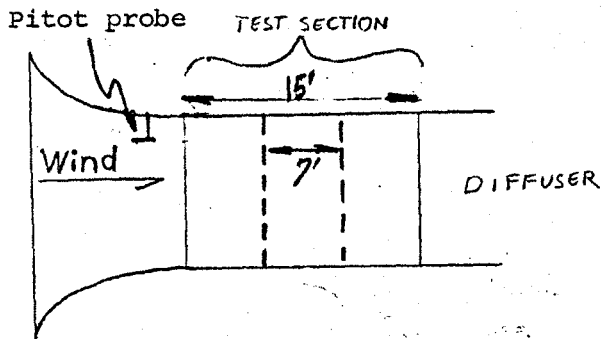
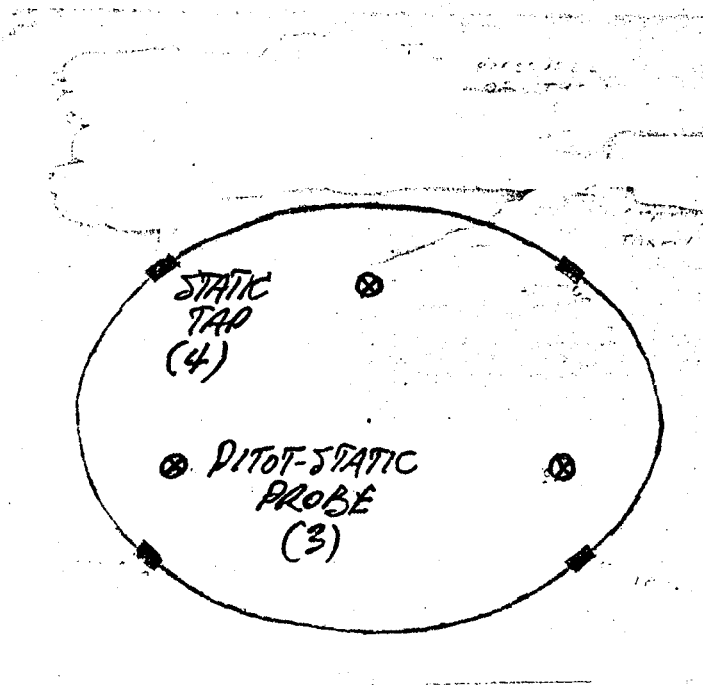


Fig. III-2a. Side view of test section showing upstream reference pitot probe and the calibration planes.



STATIC TAPS: Four taps around section as indicated; their average pressure provided the single reference static pressure.

PITOT-STATIC PROBES: Three probes in test plane.

Fig. III-2b. Cross-section of the model station test plane, showing the positions of pitot-static probes and reference static taps.

The measurement system consisted of a Type D, solenoid operated 48-tap scannivalve in combination with a model 237 ± 0.5 psi Setra pressure transducer. Plastic tubing was used between the scannivalve and the taps. A Baratron unit was also used to measure the upstream pitot pressure. Both Baratron and Setra units measured pressure differences relative to the reference static pressure (Fig. III-2b). The Setra unit was mounted on the back of the rake, with remote input and all output in wire and tubing entering through a hole in the floor (Fig. III-4).

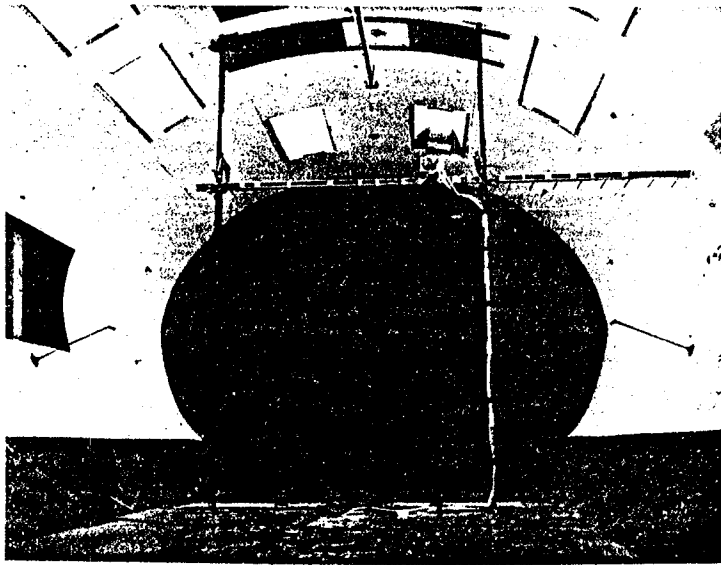


Fig. III-3. Calibration rake positioned in tunnel.

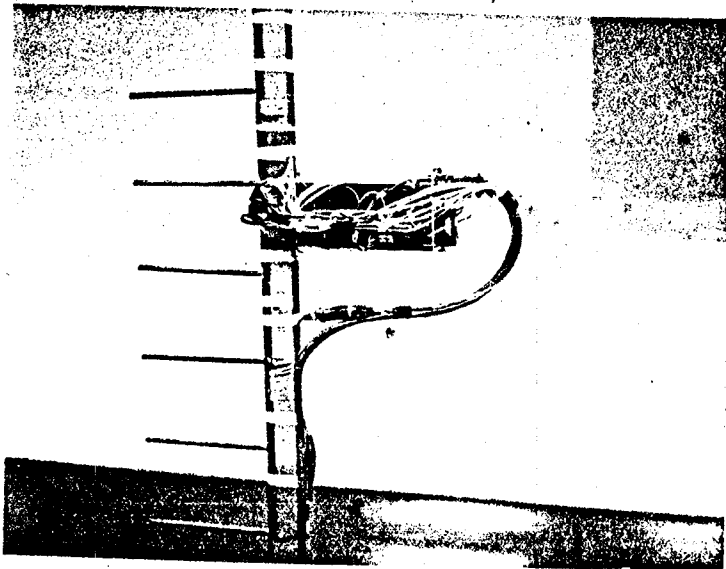


Fig. III-4. Photograph of scannivalve and Setra transducer mounted on the rake.

Twenty-nine readings were taken for each test run. Following is a table showing a breakdown of the parameter measured at each tap.

Tap Number(s)	Description of Tap Measurement
1	Reference total pressure upstream of entrance to test section (Fig. III-2a)
2 - 22	Total pressure at 21 pitot tubes on movable rake (Fig. III-3)
24, 23	Static and total pressures at pitot-static probes (Fig. III-2b) in measurement plane, near top, center.
25, 26	Static and total pressures at pitot-static probes (Fig. III-2b) in measurement plane, towards outer wall, i.e. on left facing upstream.
27, 28	Static and total pressures at pitot-static probes (Fig. III-2b) in measurement plane, towards inner wall, i.e. on right facing upstream.

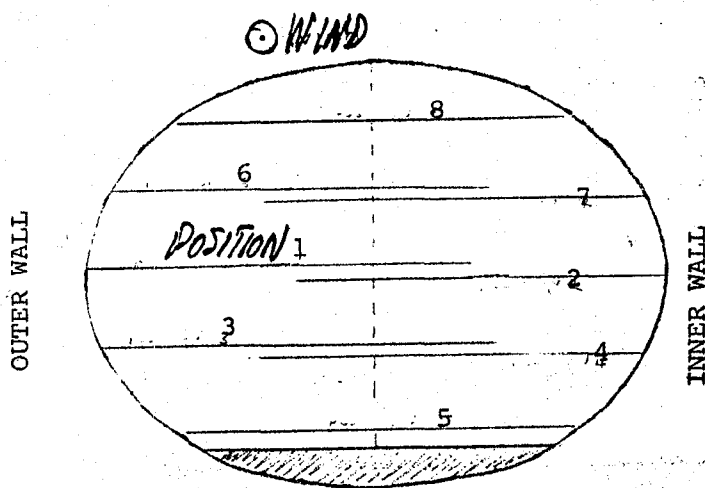
The scannivalve position was controlled and the data recorded with the aid of a computer program (WBWT1, prepared by F. H. Durgin and J. Biller) which generated as output a pressure coefficient for each tap. The total pressure (relative to reference static) measured at tap 1 was used to normalize all pressure measurements. The data were corrected for instrument offset and drift, and plotted as functions of position. Finally, contour maps were prepared to show loci of constant normalized total pressure parameters in such test planes. A map was drawn for each velocity. For a more detailed explanation of the numerical data reduction, see Appendix I.

3.1 Computer Output and Data:

During the calibration test a distinct file was generated as output for each test run. Since there were nine rake positions and five speeds, a total of 45 output files were generated. Each file for this first data plane (at the model station) is named TUNCAL.abc, including a three-digit descriptor abc. The first digit, a, of the descriptor indicates the nominal wind speed:

1	35 mph
2	50 mph
3	70 mph
4	100 mph
5	125 mph

The second digit, b, of the descriptor provides for specifying future calibrations. In this case, the second digit is always 0. The third digit of the descriptor, c, designates the position of the rake in the test plane (Fig. III-5; photographs appear in Appendix II).



At position 9, the rake was vertical in the very center, along the dotted line.

Fig. III-5. Rake positions, facing upstream.

4. Calibration Data; TUNCAL.101-509

Appendix III, Part A, contains data from the calibration carried out in the model station plane. The first three pages in the Appendix are tables of computer output. The Cp_n entries in each column are a series of normalized pressures; each column of computer output corresponds to a single test run. A more detailed explanation of the computer output and the subsequent numerical corrections for instrument shift, etc., are described in Appendix I.

Following the reduced data are six pages of graphs (App. III, Part B) showing normalized total pressure parameters as a function of position in the test plane. Positions 1 and 2, positions 3 and 4, and positions 6 and 7 share pages respectively (see Fig. III-5). There are five graphs included on each page, one for each velocity.

Finally, there are five contour maps, one for each speed, showing contours of constant total pressure parameter (App. III, Part C). These maps are based on interpolations from the graphs of total pressure parameters with respect to position.

5. Calibration of Test Section, Second Measurement Plane

This series of test runs was identical in purpose to the series at the model station (Section 3) excepting that the rake and the pitot-static probes were positioned in a second test plane located seven feet downstream of the

model station (Fig. III-2a). Test runs were performed at only three speeds, and, unfortunately, the fourth and ninth rake positions were omitted due to a tunnel accident.

The output data file names for this series of test runs were of the format TUNCA2.abc including a three-digit descriptor following. As before, the first digit of the extension indicates velocity and the last refers to rake position (Fig. III-5). For this series, the second digit is always 4.

Note that the upstream total and the four wall static reference taps (i.e. taps 1 and the average on 48) were not moved for the second test series. Those measurements refer as before to the same tunnel locations (Fig. III-2a,b).

The data for this second test series appears in Appendix IV, Parts A, B and C.

6. Conclusion

Parts B and C of Appendices III and IV indicate the following:

A. Dynamic pressure distributions across test section are in most cases within $\pm 1\%$ over half the span, and for speeds in the range 50 to 100 mph.

B. A bias towards higher/lower speeds on the inner/outer sides (i.e. right/left in figures) is apparent near the horizontal midplane (position pairs 1, 2; 3, 4; and 6, 7). The contours drawn in Part C illustrate the relatively accelerated regions (larger C_{p_n}) more clearly.

C. The vertical survey (position 9) shows quite flat variations along the vertical midplane. In combination with the horizontal surveys, a slight antisymmetry about the vertical midplane is present but with a useful central core flow representing about 0.75 of the horizontal/vertical spans.

APPENDIX I

DATA REDUCTION

Two measurement systems were used during the program. A Setra pressure transducer connected to a scannivalve was used for all taps. A Baratron unit also was used for the upstream pitot (tap 1) and its indicated pressures were used as a basis for normalizing all other readings. Both Setra and Baratron units were referenced to the average static pressure in the model plane (first calibration) as determined from the four wall taps around the tunnel boundary (recorded as tap 48).

Define:

$$\begin{aligned}
 p_{t \text{ REF}} & \text{ total pressure at upstream pitot (tap 1)} \\
 p_{s \text{ REF}} & \text{ static pressure average based on four wall taps in} \\
 & \text{ model plane (tap 48)} \\
 p_n & \text{ pressure, total or static, at tap n} \\
 & \text{(see description, p 8)} \\
 q_{\text{REF}} & \text{ reference dynamic pressure } (p_{t \text{ REF}} - p_{s \text{ REF}})
 \end{aligned} \tag{1}$$

The pressure transducers (Setra and Baratron) are referenced to indicate increments above $p_{s \text{ REF}}$. Thus

$$\begin{aligned}
 p_{\text{BARA}} & = p_{t \text{ REF}} - p_{s \text{ REF}} \quad (\equiv q_{\text{REF}}) \quad \text{(for tap 1)} \\
 (p_{\text{SETR}})_n & = p_n - p_{s \text{ REF}} \quad \text{(for tap n)}
 \end{aligned} \tag{2}$$

if the instrument systems were perfect. Actually there are errors due to initial offset and zero drift during the measurement procedures.

Say

$$(p_{s \text{ REF}})_{\text{Apparent}} = p_{s \text{ REF}} + \Delta p_{\text{OFFSET}} + \Delta p_{\text{DRIFT}} \tag{3}$$

in which the offset and drift contributions may differ for different transducers. Then the recorded values would be

$$\begin{aligned}
 p'_{\text{BARA}} & = q_{\text{REF}} - (\Delta p_{\text{OFFSET}} + \Delta p_{\text{DRIFT}})_{\text{BARA}} \\
 (p'_{\text{SETR}})_n & = (p_{\text{SETR}})_n - (\Delta p_{\text{OFFSET}} + \Delta p_{\text{DRIFT}})_{\text{SETR}}
 \end{aligned} \tag{4}$$

The value of $(p_{\text{SETR}})_{48I}$ prior to a data scan establishes $(\Delta p_{\text{OFFSET}})_{\text{SETR}}$ since the initial drift is zero by definition. I.e. from eq.(4b)*

$$(p'_{\text{SETR}})_{48I} = -(\Delta p_{\text{OFFSET}})_{\text{SETR}} \tag{5}$$

*This initial zero reading is not included in the tables.

and has been used to remove that tare from all of the Setra data. [Subscript 48I refers to the "initial" tap 48 reading.] The drift contribution to the Baratron readings is known to be small and it is assumed here that

$$(\Delta p_{\text{DRIFT}})_{\text{BARA}} = 0 \quad (6)$$

Now eq.(4), with (5) and (6), becomes

$$p''_{\text{BARA}} = q_{\text{REF}} - (\Delta p_{\text{OFFSET}})_{\text{BARA}} \quad [= p'_{\text{BARA}}] \quad (7)$$

$$(p''_{\text{SETR}})_n = (p_{\text{SETR}})_n - (\Delta p_{\text{DRIFT}})_{\text{SETR}} \quad (= (p'_{\text{SETR}})_n - (p'_{\text{SETR}})_{48I})$$

and we define an uncorrected, normalized pressure coefficient to be

$$Cp_n = \frac{(p''_{\text{SETR}})_n}{(p''_{\text{BARA}})} \quad (8)$$

Cp_n is tabulated in Parts A of Appendices III and IV for the data that was recorded for the two calibration planes.

SETRA Drift Correction

The last read tap 48 outputs shown in the Appendices indicate the total drifts during a given scan, i.e. from eq.(7)

$$(p''_{\text{SETR}})_{48} = -(\Delta p_{\text{DRIFT}})_{\text{SETR,TOTAL}} \quad (9)$$

The correction will assume that drift is linear with time. Since the scan is also sequentially linear over all $N(= 29)$ taps,

$$(\Delta p_{\text{DRIFT}})_{\text{SETR},n} = \frac{n}{N} (-p''_{\text{SETR}})_{48} \quad (10)$$

Then

$$Cp'_n = \frac{(p_{\text{SETR}})_n}{p''_{\text{BARA}}} = Cp_n + \frac{(\Delta p_{\text{DRIFT}})_{\text{SETR}}}{p''_{\text{BARA}}}$$

$$= Cp_n - \frac{n}{N} Cp_{48} \quad (11)$$

and is a value corrected for drift.

Baratron Offset Correction

From Eqs. (11), (7) and (2), for tap 1:

$$Cp'_1 = \frac{(p_{SETR})_1}{q_{REF} - (\Delta p_{OFFSET})_{BARA}} = \frac{1}{1 - \left(\frac{(\Delta p_{OFFSET})_{BARA}}{q_{REF}} \right)} \quad (12)$$

and the offset correction is implied by the difference from unity of Cp'_1 .
Eq. (11) may now be written as

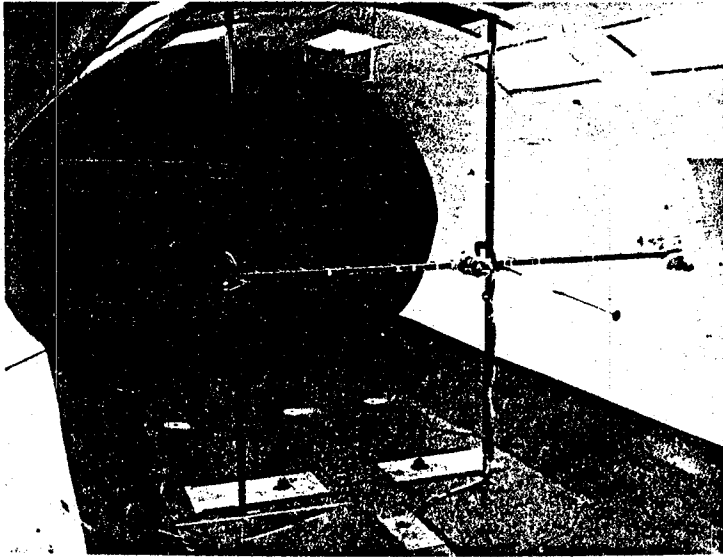
$$Cp'_n = \frac{(p_{SETR})_n}{q_{REF}} Cp'_1 \quad (13)$$

or

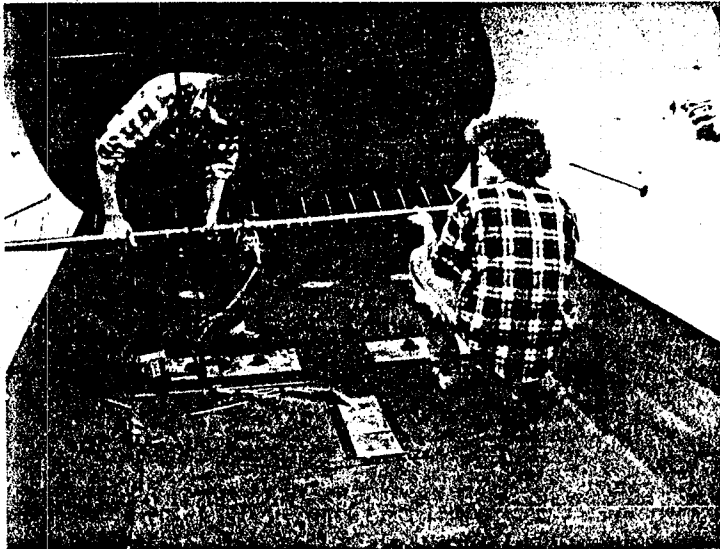
$$Cp''_n = \frac{(p_{SETR})_n}{q_{REF}} = \frac{Cp'_n}{Cp'_1} = \frac{Cp_n - \frac{n}{N} Cp_{48}}{Cp_1 - \frac{1}{N} Cp_{48}} \quad (14)$$

is a fully corrected pressure coefficient corresponding to a ratio of the "perfect" differences defined in Eq. (2). The normalized, corrected, pressure coefficient Cp''_n has been found from the tables in Appendices III and IV and is plotted and contoured (after interpolation) in Parts B and C of those Appendices.

APPENDIX II: Photographs of selected rake positions.

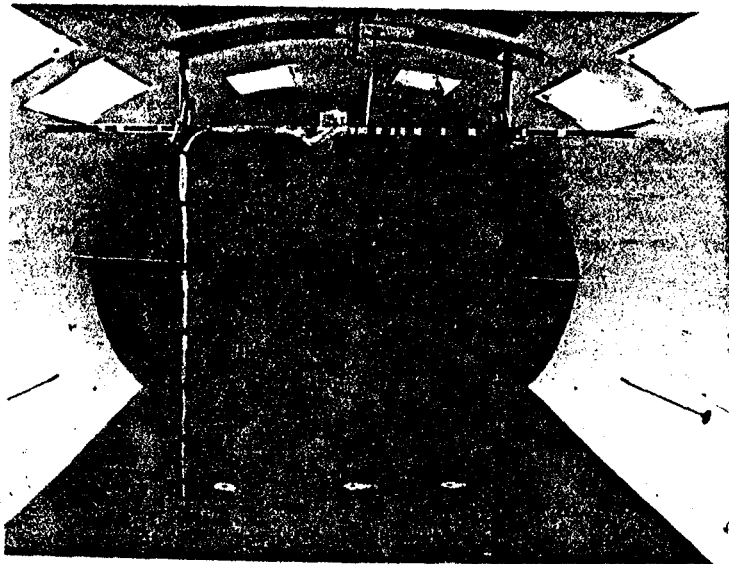
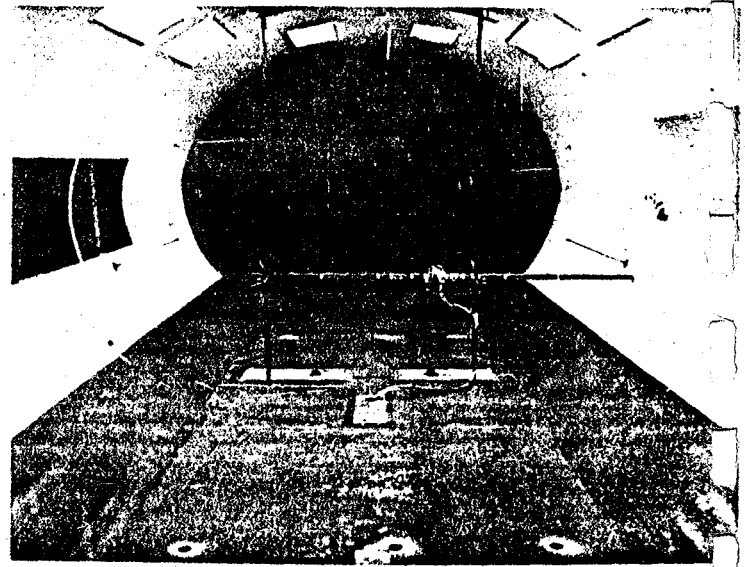


Rake position 2



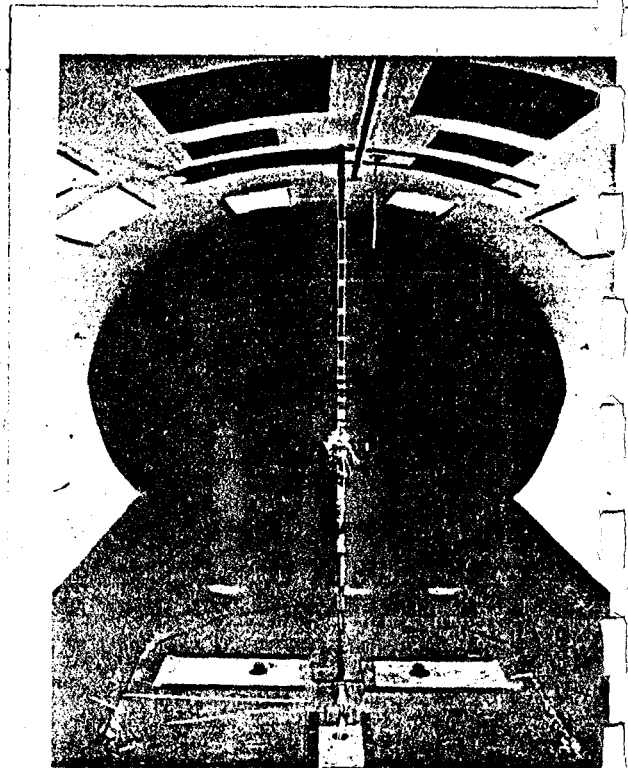
Rake position 3

Rake position 4
(Looking upstream)



Rake position 8

Rake position 9



APPENDIX III, Part A

Uncorrected Calibration Data for TUNCAL.abc Files, First (Model Station) Plane

FILE.abc Vel.,mph	.101	.102	.103	.104	.105	.106	.107	.108	.109	.201	.202	.203	.204	.205	.206	.207
TAP	C _{Pn}															
1	1.063	1.047	1.038	1.053	1.059	1.078	1.073	1.069	1.073	1.022	1.022	1.015	1.023	1.029	1.029	1.026
2	0.991	1.041	0.984	1.043	1.014	1.033	1.063	1.041	0.910	0.948	1.021	0.994	1.011	0.977	0.992	1.025
3	1.030	1.002	1.031	1.044	1.039	1.032	1.001	1.002	1.067	0.995	1.022	0.999	1.014	1.007	1.007	1.026
4	1.031	0.994	1.039	1.042	1.043	1.038	1.057	1.001	1.075	0.991	1.013	1.013	1.012	1.006	1.017	1.022
5	0.998	1.028	1.030	1.041	1.032	1.064	1.069	1.064	1.079	0.992	1.015	1.007	1.025	1.013	1.018	1.028
6	1.021	1.043	1.023	1.033	1.030	1.059	1.066	1.064	1.069	1.001	1.015	1.006	1.032	1.016	1.010	1.027
7	1.018	1.026	1.007	1.052	1.030	1.053	1.062	1.062	1.068	1.012	1.024	1.007	1.030	1.020	1.022	1.018
8	1.017	1.059	1.025	1.046	1.051	1.056	1.066	1.063	1.066	1.023	1.018	1.009	1.028	1.012	1.021	1.030
9	1.017	1.076	1.011	1.044	1.033	1.063	1.054	1.065	1.067	1.026	1.018	1.014	1.023	1.021	1.021	1.033
10	1.015	1.048	1.030	1.043	1.057	1.040	1.033	1.065	1.067	1.018	1.019	1.018	1.029	1.015	1.023	1.038
11	1.005	1.014	1.006	1.041	1.048	1.027	1.062	1.065	1.059	1.026	1.031	1.013	1.029	1.024	1.011	1.031
12	0.996	1.000	1.000	1.041	1.037	1.032	1.034	1.062	1.061	1.023	1.023	1.018	1.031	1.022	1.016	1.034
13	0.996	1.037	0.992	1.016	1.024	1.032	1.030	1.059	1.052	1.012	1.022	1.013	1.020	1.017	1.023	1.034
14	0.993	1.041	0.992	1.014	1.032	1.029	1.031	1.053	1.045	1.014	1.027	1.022	1.033	1.019	1.017	1.036
15	0.996	1.022	0.978	1.032	1.030	1.030	1.028	1.063	1.045	1.019	1.025	1.020	1.039	1.025	1.021	1.040
16	1.000	1.058	0.995	1.028	1.033	1.029	1.047	1.041	1.043	1.024	1.027	1.024	1.035	1.026	1.021	1.037
17	0.996	1.060	0.989	1.031	1.035	1.030	1.044	1.056	1.044	1.027	1.031	1.023	1.036	1.027	1.026	1.053
18	1.012	1.041	0.991	1.027	1.034	1.017	1.056	1.038	1.041	1.018	1.024	1.023	1.041	1.026	1.024	1.046
19	0.982	1.040	0.992	1.015	1.039	1.047	1.048	1.040	1.047	1.026	1.025	1.007	1.045	1.032	1.024	1.047
20	1.010	1.057	1.005	1.034	1.036	1.019	1.053	1.055	1.037	1.036	1.018	1.019	1.042	1.041	1.030	1.051
21	1.019	1.037	0.983	1.009	1.041	1.020	1.017	1.062	0.991	1.032	1.003	1.021	1.041	1.021	1.029	1.027
22	1.012	0.881	0.971	0.985	1.005	1.024	0.899	1.040	0.858	1.027	0.882	1.021	0.984	0.991	1.031	0.966
23	0.993	1.027	0.979	1.018	1.021	1.037	1.005	1.046	1.027	1.004	1.013	1.013	1.023	1.020	1.018	1.027
24	-0.054	-0.032	-0.070	-0.049	-0.032	-0.053	-0.064	0.005	-0.045	-0.012	-0.012	-0.009	-0.008	-0.005	-0.009	-0.006
25	-0.057	-0.050	-0.074	-0.065	-0.049	-0.069	-0.081	-0.052	-0.068	-0.009	-0.021	-0.009	-0.014	-0.018	-0.023	-0.017
26	0.964	1.019	0.966	0.996	1.006	1.017	1.003	1.037	1.016	1.003	0.998	1.001	1.018	1.008	1.009	1.017
27	-0.053	-0.038	-0.079	-0.044	-0.041	-0.062	-0.074	-0.047	-0.067	-0.009	-0.002	-0.012	0.006	0.010	-0.009	-0.008
28	1.011	1.044	0.991	1.021	1.038	1.055	1.037	1.068	1.053	1.030	1.024	1.036	1.044	1.044	1.044	1.045
48	-0.057	-0.045	-0.080	-0.057	-0.039	-0.068	-0.076	-0.043	-0.066	-0.008	-0.010	-0.007	-0.002	-0.005	-0.008	-0.006

NOTE: Three-digit descriptor .abc in file identifications of form TUNCAL.abc
 Designate: rake position by last digit (c), tunnel speed by first digit (a) [1,2,3,4,5 nominally 35,50,70,100,140 mph]

APPENDIX III, Part A (continued)

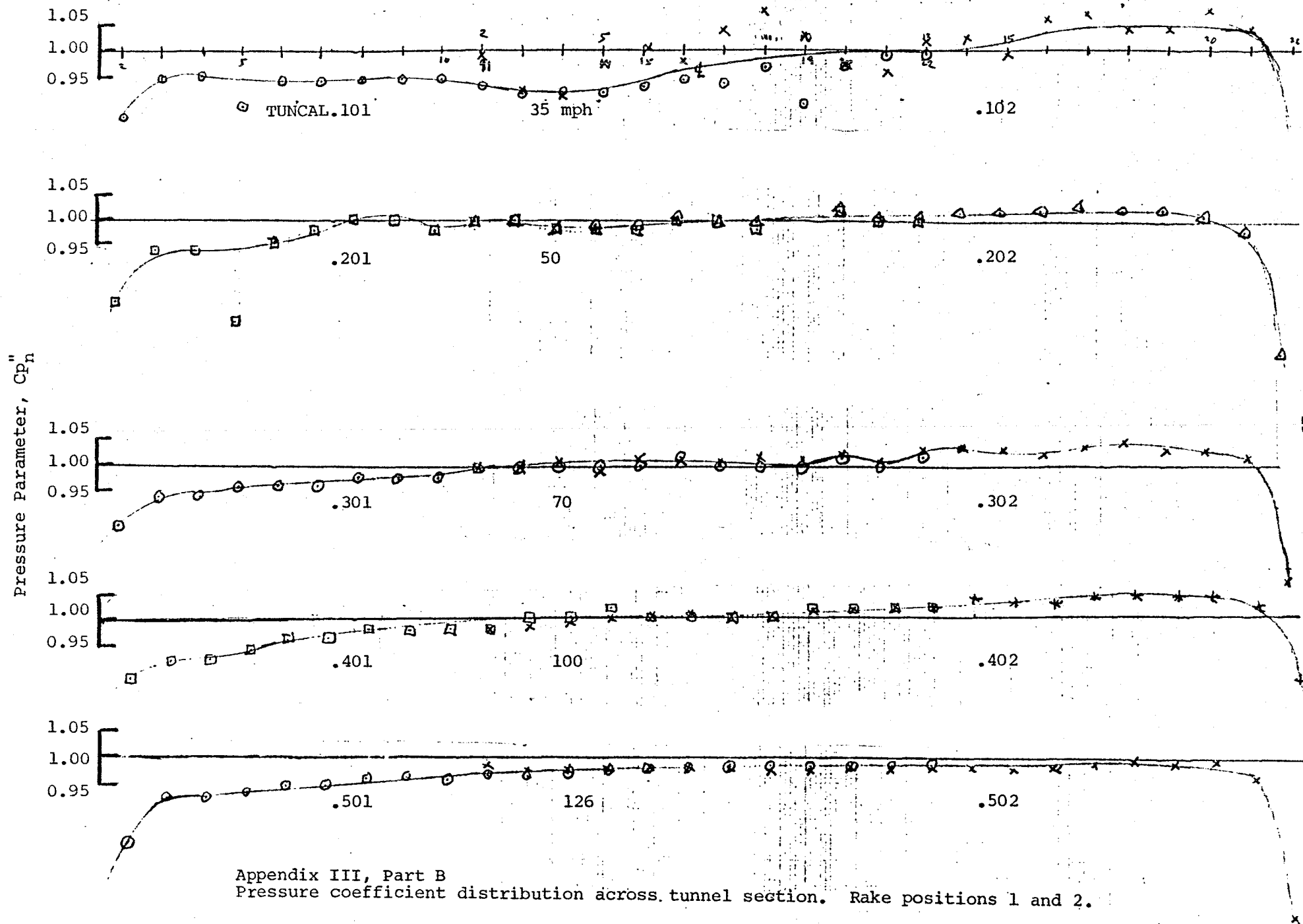
Uncorrected Calibration Data for TUNCAL,abc Files First (Model Station) Plane

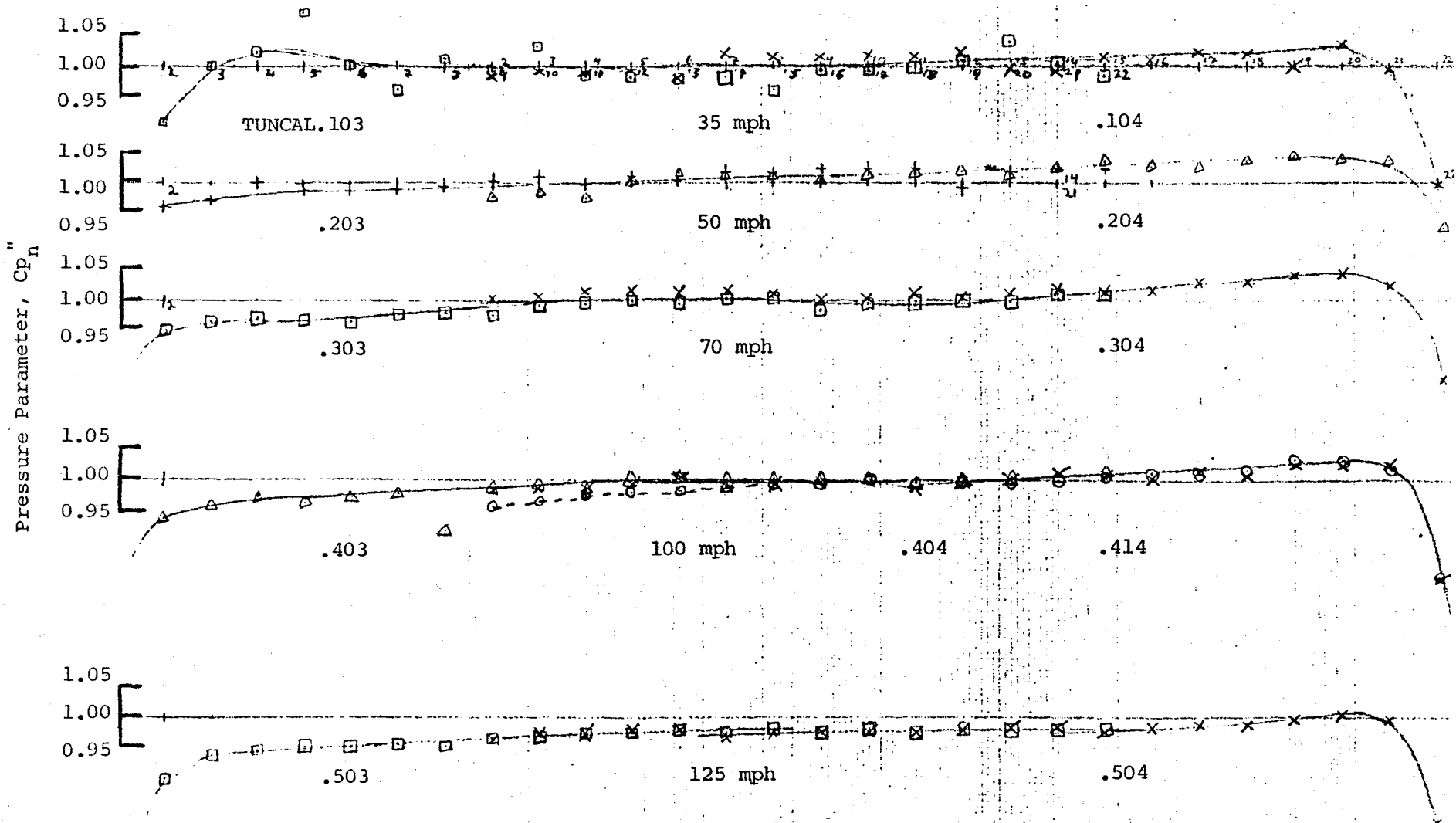
FILE,abc	.208	.209	.301	.302	.303	.304	.305	.306	.307	.308	.309	.401	.402	.403	.404	.414
Vel.,mph	48.6	48.9	70.3	69.8	70.2	69.4	69.7	69.1		69.7	70.	98.8	99	98.5	99.7	98.3
TAP	Cp _n															
1	1.023	1.023	1.008	1.005	1.007	1.010	1.013	1.009	1.011	1.007	1.011	1.006	1.000	1.009	1.009	1.011
2	0.986	0.912	0.947	1.004	0.982	1.011	0.976	0.970	1.011	0.982	0.884	0.949	0.988	0.977	0.987	1.003
3	1.000	1.025	0.981	1.004	0.989	1.013	0.992	0.985	1.012	1.002	1.005	0.968	0.992	0.987	0.993	1.004
4	1.009	1.033	0.973	1.008	0.992	1.017	0.997	0.988	1.012	0.997	1.005	0.970	0.994	0.995	0.998	1.005
5	1.013	1.024	0.989	1.002	0.990	1.020	1.000	0.994	1.015	1.002	1.008	0.981	0.999	0.990	0.999	1.008
6	1.013	1.037	0.988	1.015	0.988	1.018	0.999	0.996	1.013	0.997	1.011	0.983	1.000	0.994	1.001	1.012
7	1.015	1.032	0.991	1.011	0.996	1.019	1.002	1.000	1.017	1.000	1.013	0.989	1.003	0.997	1.007	1.006
8	1.015	1.033	0.998	1.010	0.997	1.015	1.001	1.000	1.018	1.002	1.003	0.997	1.001	1.003	1.006	1.007
9	1.016	1.037	0.999	1.015	0.995	1.010	1.002	1.001	1.021	1.003	1.017	0.998	1.006	1.005	1.011	1.009
10	1.017	1.036	1.002	1.015	1.003	1.012	1.005	1.003	1.016	1.007	1.017	0.998	1.006	1.005	1.011	1.009
11	1.027	1.030	1.004	1.018	1.004	1.016	1.004	1.004	1.023	1.002	1.015	0.999	1.007	1.003	1.005	1.005
12	1.026	1.030	1.004	1.012	1.006	1.011	1.005	1.006	1.027	1.008	1.017	1.002	1.011	1.010	1.009	1.009
13	1.023	1.035	1.005	1.023	1.004	1.016	1.005	1.009	1.027	1.008	1.015	1.003	1.011	1.010	1.008	1.011
14	1.023	1.032	1.012	1.024	1.009	1.022	1.006	1.012	1.032	1.009	1.017	1.012	1.019	1.011	1.010	1.017
15	1.016	1.028	1.008	1.023	1.009	1.018	1.013	1.014	1.031	1.011	1.016	1.010	1.015	1.011	1.014	1.013
16	1.035	1.029	1.017	1.017	1.000	1.020	1.011	1.021	1.031	1.015	1.014	1.008	1.014	1.011	1.016	1.014
17	1.027	1.029	1.012	1.024	1.004	1.026	1.020	1.020	1.035	1.011	1.013	1.010	1.020	1.011	1.016	1.017
18	1.029	1.024	1.013	1.025	1.007	1.026	1.014	1.019	1.032	1.015	1.014	1.006	1.020	1.007	1.020	1.016
19	1.035	1.016	1.013	1.020	1.007	1.032	1.019	1.019	1.038	1.017	1.011	1.013	1.010	1.010	1.027	1.025
20	1.035	1.008	1.014	1.021	1.006	1.034	1.018	1.022	1.028	1.016	0.991	1.014	1.019	1.012	1.027	1.024
21	1.042	1.012	1.013	1.013	1.013	1.024	1.017	1.021	1.018	1.003	1.001	1.016	1.008	1.013	1.020	1.024
22	1.026	0.864	1.018	0.889	1.012	0.942	0.989	1.027	0.973	1.017	0.888	1.018	0.938	1.016	0.929	0.928
23	1.026	1.024	1.006	1.001	1.003	1.014	1.012	1.011	1.015	1.009	1.009	1.006	1.006	1.011	1.010	1.010
24	0.040	0.006	-0.004	-0.003	-0.004	0.001	0.001	-0.002	-0.001	0.041	0.013	-0.000	0.001	-0.000	0.002	0.001
25	-0.021	-0.010	-0.006	-0.014	-0.004	-0.014	-0.014	-0.017	-0.015	-0.021	-0.013	-0.004	-0.013	-0.002	-0.011	-0.015
26	1.019	1.014	0.992	0.992	0.987	0.991	0.990	0.994	0.993	0.980	0.995	0.985	0.978	0.986	0.991	0.987
27	-0.008	-0.013	-0.003	0.003	-0.007	0.009	-0.005	-0.003	-0.005	-0.004	-0.006	0.006	0.010	-0.001	0.015	0.011
28	1.061	1.040	1.029	1.022	1.026	1.032	1.036	1.031	1.031	1.024	1.039	1.026	1.010	1.031	1.031	1.028
48	-0.003	-0.007	-0.001	-0.000	-0.001	0.000	-0.000	0.000	-0.002	-0.001	-0.001	0.002	0.001	0.002	0.003	0.000

APPENDIX III, Part A (continued)

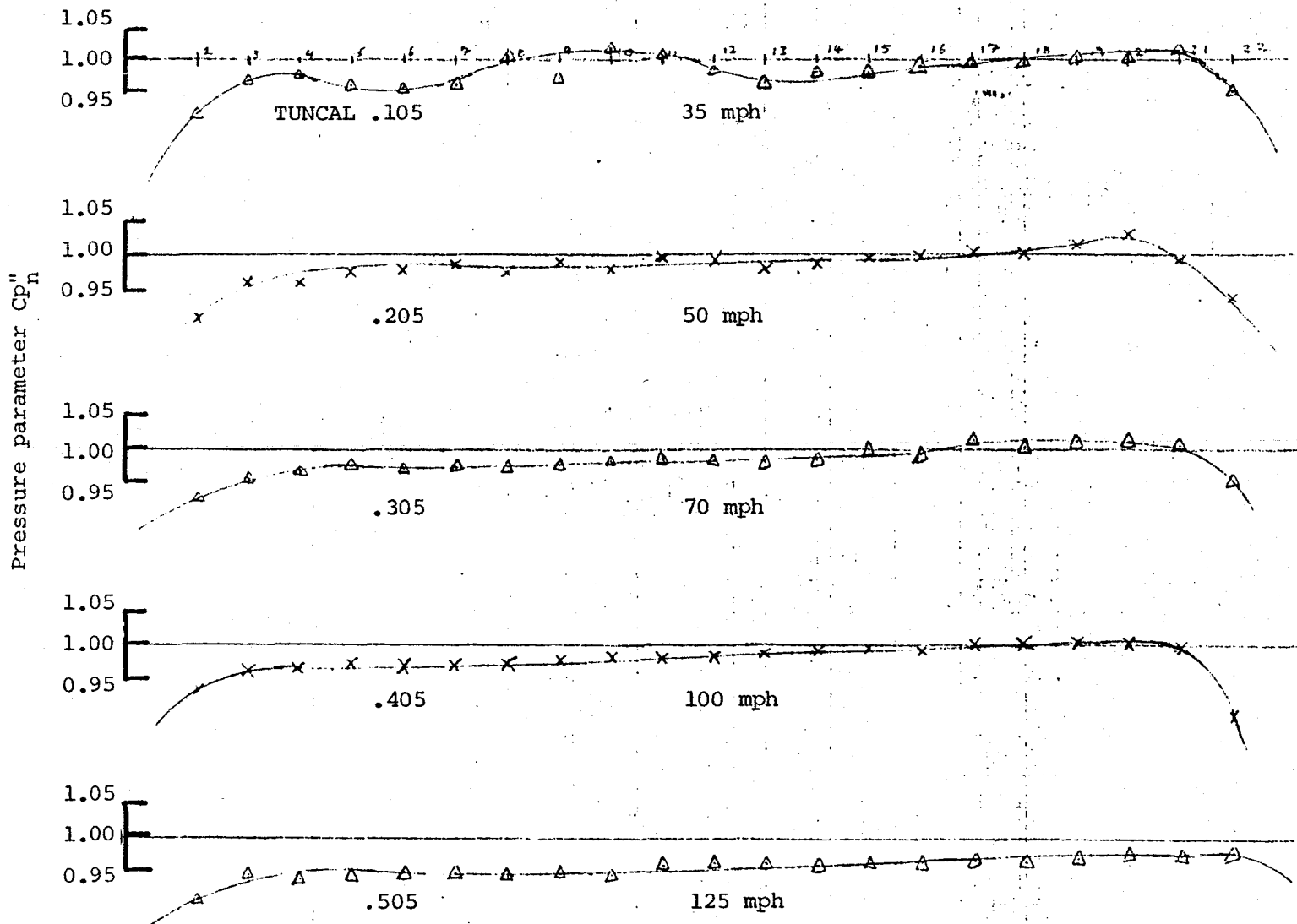
Uncorrected Calibration Data for TUNCAL.abc Files, First (Model Station) Plane

FILE.abc Vel.,mph TAP	.405 98.9	.406 99.5	.407 99.7	.408 100.	.409 100.	.501 125.8	.502 124.5	.503 125.	.504 124.9	.505 124.3	.506 125.	.507 124.8	.508 125.1	.509 124.7
	Cp _n													
1	1.007	1.003	1.004	1.002	1.004	1.007	1.004	1.009	1.009	1.010	1.005	1.003	1.002	1.004
2	0.972	0.958	1.000	0.978	0.914	0.920	0.997	0.957	0.991	0.963	0.947	0.987	0.969	0.908
3	0.987	0.980	1.001	0.993	0.996	0.966	0.993	0.977	0.996	0.982	0.976	0.994	0.981	0.985
4	0.988	0.986	1.002	0.993	0.999	0.966	0.994	0.982	0.997	0.979	0.979	0.993	0.986	0.986
5	0.992	0.988	1.002	0.993	1.003	0.971	0.994	0.984	0.999	0.982	0.981	0.995	0.986	0.991
6	0.992	0.988	1.000	0.995	1.004	0.979	0.993	0.984	0.998	0.984	0.983	0.998	0.990	0.994
7	0.991	0.991	1.009	0.995	1.003	0.979	0.994	0.987	0.994	0.984	0.988	0.998	0.991	0.992
8	0.993	0.994	1.015	0.999	1.004	0.987	0.993	0.985	0.998	0.981	0.988	0.999	0.993	0.991
9	0.996	0.996	1.015	0.999	1.004	0.987	0.991	0.992	0.998	0.983	0.991	0.999	0.996	0.993
10	0.999	0.995	1.015	1.001	1.007	0.985	0.992	0.995	0.997	0.982	0.992	1.001	1.002	0.992
11	0.997	0.995	1.019	1.002	1.006	0.991	0.997	0.997	0.997	0.990	0.994	1.001	1.002	0.995
12	0.999	0.999	1.020	1.005	1.010	0.990	0.993	0.998	1.000	0.991	0.997	1.001	1.002	0.990
13	1.001	1.004	1.018	1.007	1.012	0.994	0.996	1.000	1.001	0.992	0.999	1.002	1.003	0.996
14	1.003	1.006	1.021	1.001	1.009	0.996	0.996	0.998	1.002	0.990	0.998	1.004	1.004	0.996
15	1.004	1.009	1.023	1.008	1.012	0.997	0.994	1.000	0.999	0.991	0.999	1.002	1.003	1.000
16	1.004	1.012	1.026	1.005	1.011	0.998	0.997	0.997	1.001	0.992	1.001	1.005	1.001	1.002
17	1.000	1.013	1.029	1.006	1.007	0.999	1.000	1.002	1.004	0.995	1.001	1.002	1.000	1.003
18	1.009	1.014	1.026	1.004	1.003	1.000	1.003	1.000	1.006	0.994	0.998	1.005	0.998	1.004
19	1.011	1.013	1.032	1.007	1.005	1.000	1.000	1.001	1.010	0.996	1.000	1.005	0.998	1.005
20	1.008	1.019	1.029	1.007	0.995	0.999	1.002	1.001	1.014	1.000	1.001	1.003	0.998	0.997
21	1.006	1.018	1.020	1.004	0.991	1.001	0.986	1.001	1.009	0.999	1.000	0.999	0.990	0.986
22	0.954	1.022	0.962	0.986	0.897	1.001	0.853	1.002	0.922	1.001	1.001	0.919	0.956	0.894
23	1.011	1.005	1.004	1.005	1.009	1.009	1.002	1.012	1.015	1.010	1.006	1.005	1.008	1.007
24	0.004	0.001	0.003	0.044	0.017	0.005	0.008	0.006	0.008	0.005	0.004	0.006	0.046	0.020
25	-0.016	-0.017	-0.011	-0.020	-0.011	-0.005	-0.012	-0.002	-0.013	-0.015	-0.015	-0.014	-0.017	-0.012
26	0.989	0.982	0.988	0.982	0.980	0.980	0.972	0.977	0.981	0.974	0.973	0.977	0.974	0.973
27	-0.000	0.003	0.003	0.002	0.001	0.009	0.016	0.005	0.018	0.003	0.005	0.005	0.003	0.004
28	1.028	1.023	1.026	1.019	1.022	1.011	1.007	1.013	1.011	1.009	1.006	1.008	1.006	1.008
48	0.001	0.002	0.002	0.001	0.001	0.002	0.002	0.003	0.003	0.001	0.002	0.002	0.002	0.001

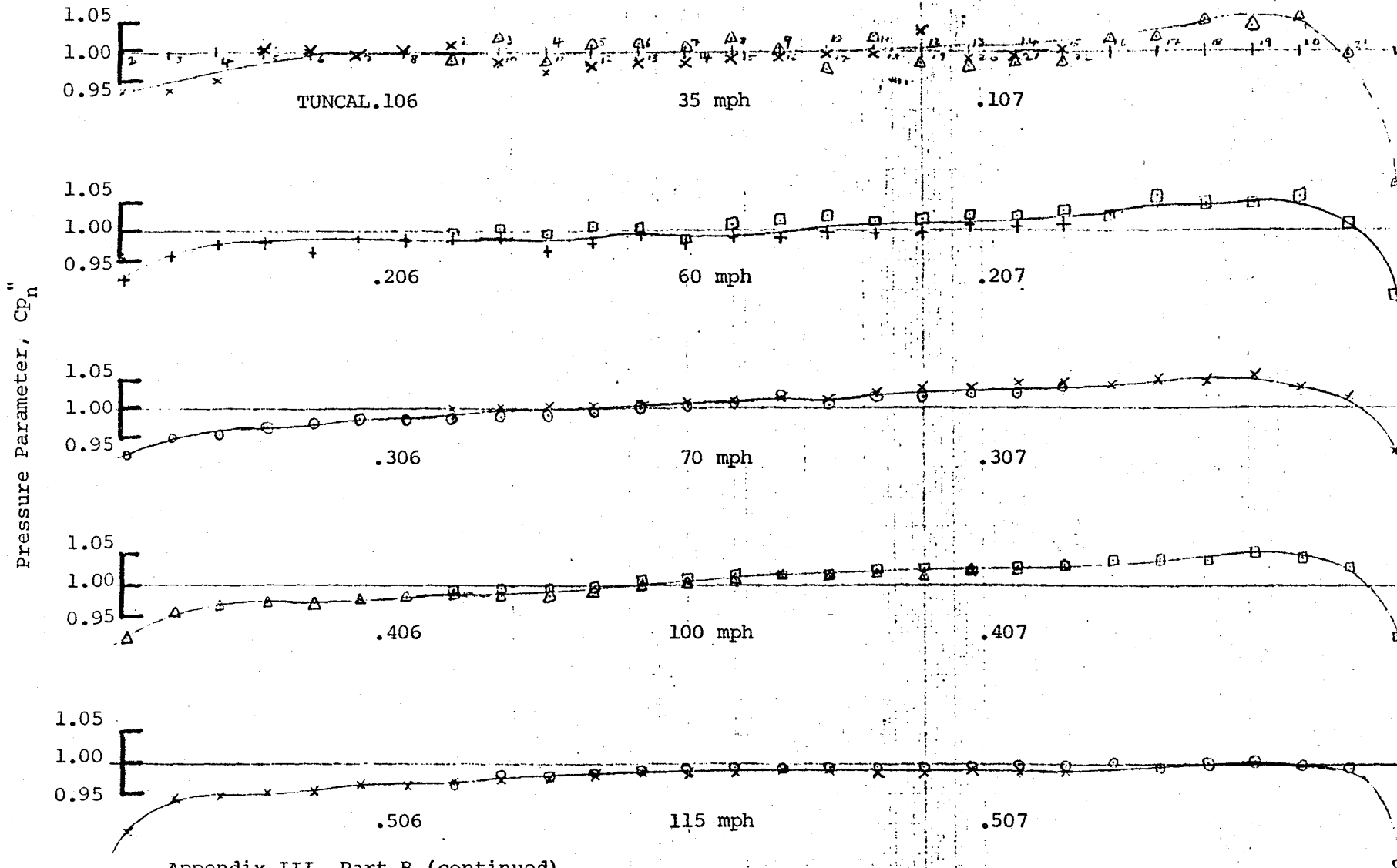




Appendix III, Part B (continued)
 Pressure coefficient distribution across tunnel section. Rake positions 3 and 4.

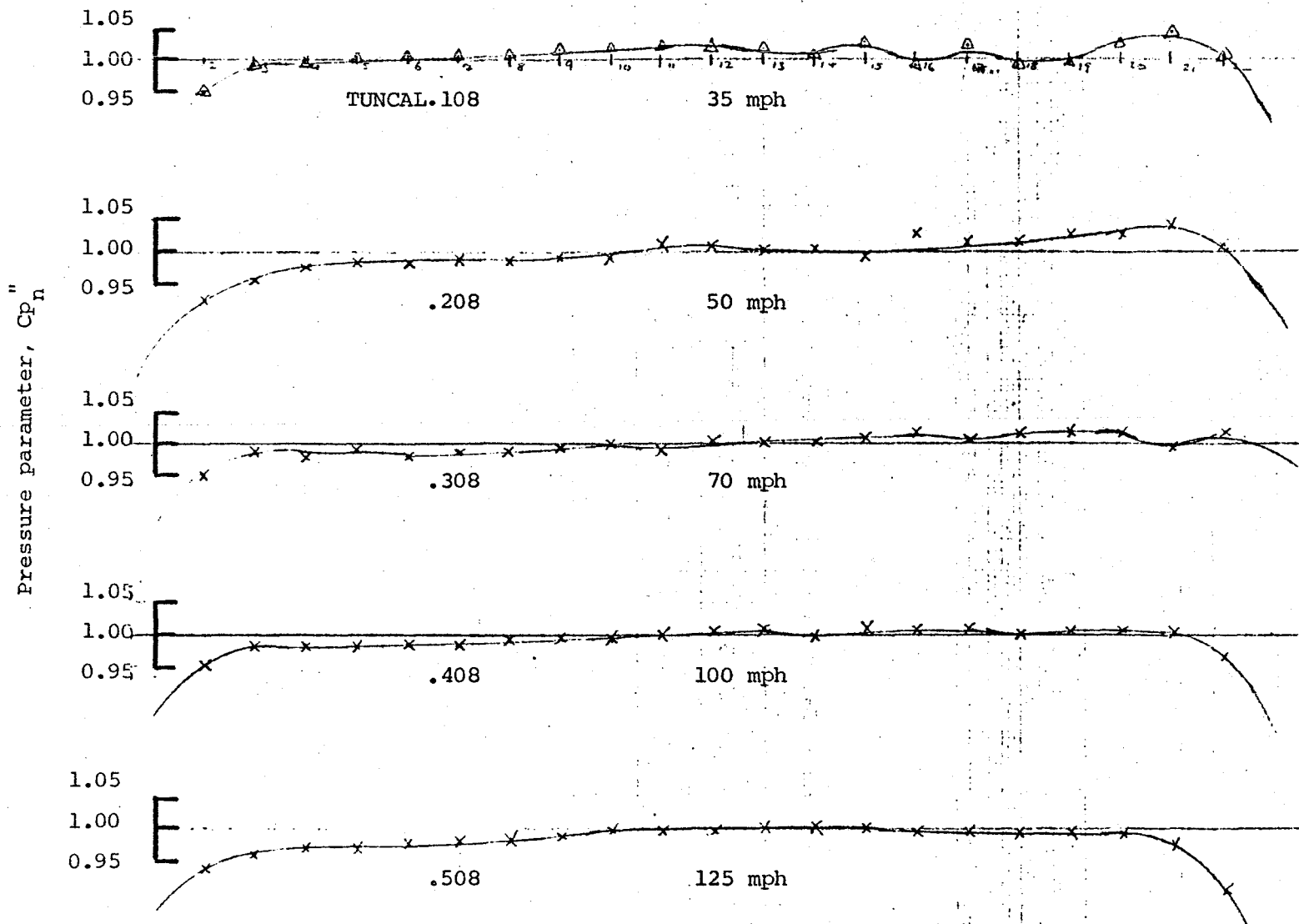


Appendix III, Part B (continued)
 Pressure coefficient distribution across tunnel section. Rake position 5.



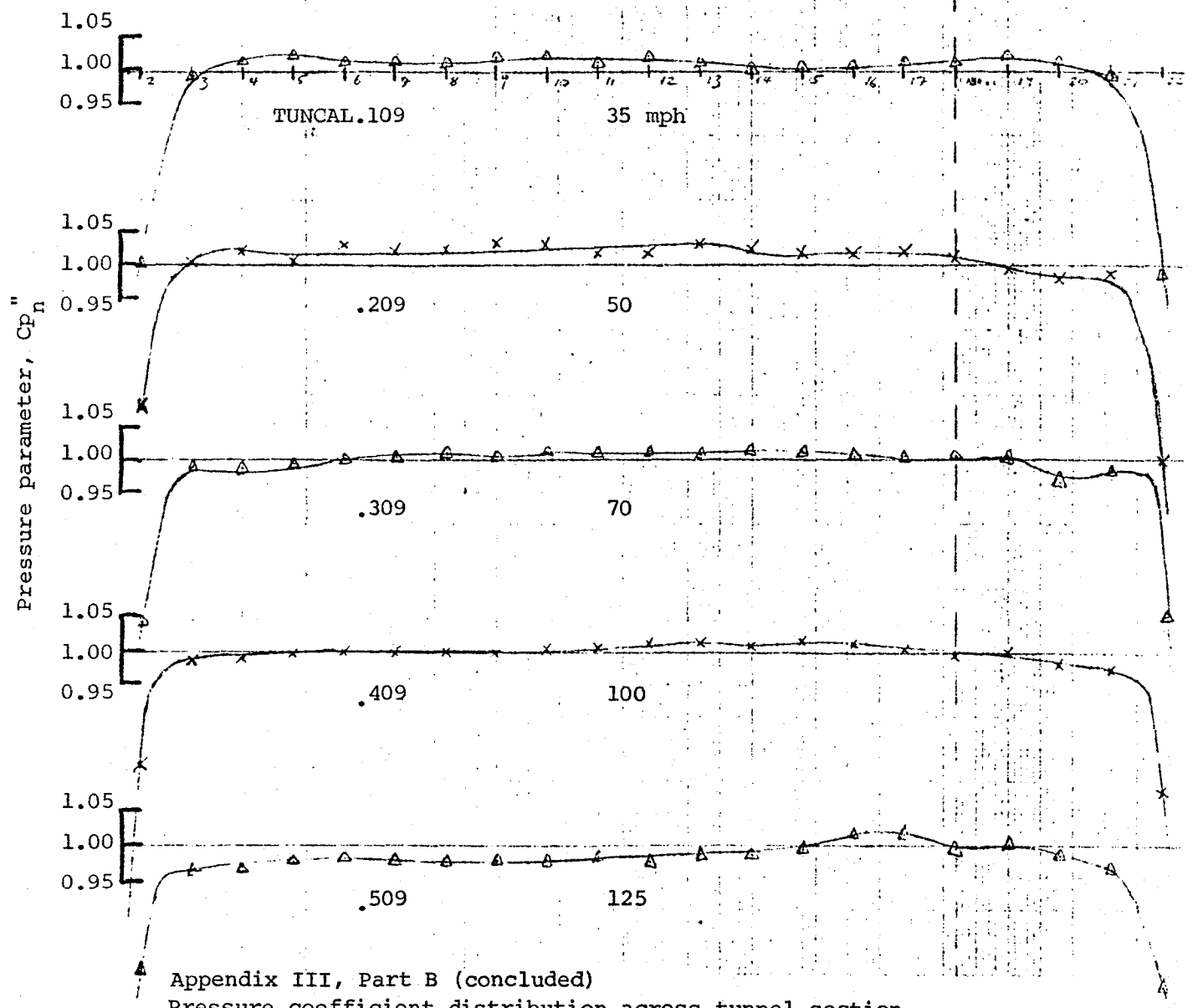
Appendix III, Part B (continued)

Pressure coefficient distribution across tunnel section. Rake positions 6 and 7.

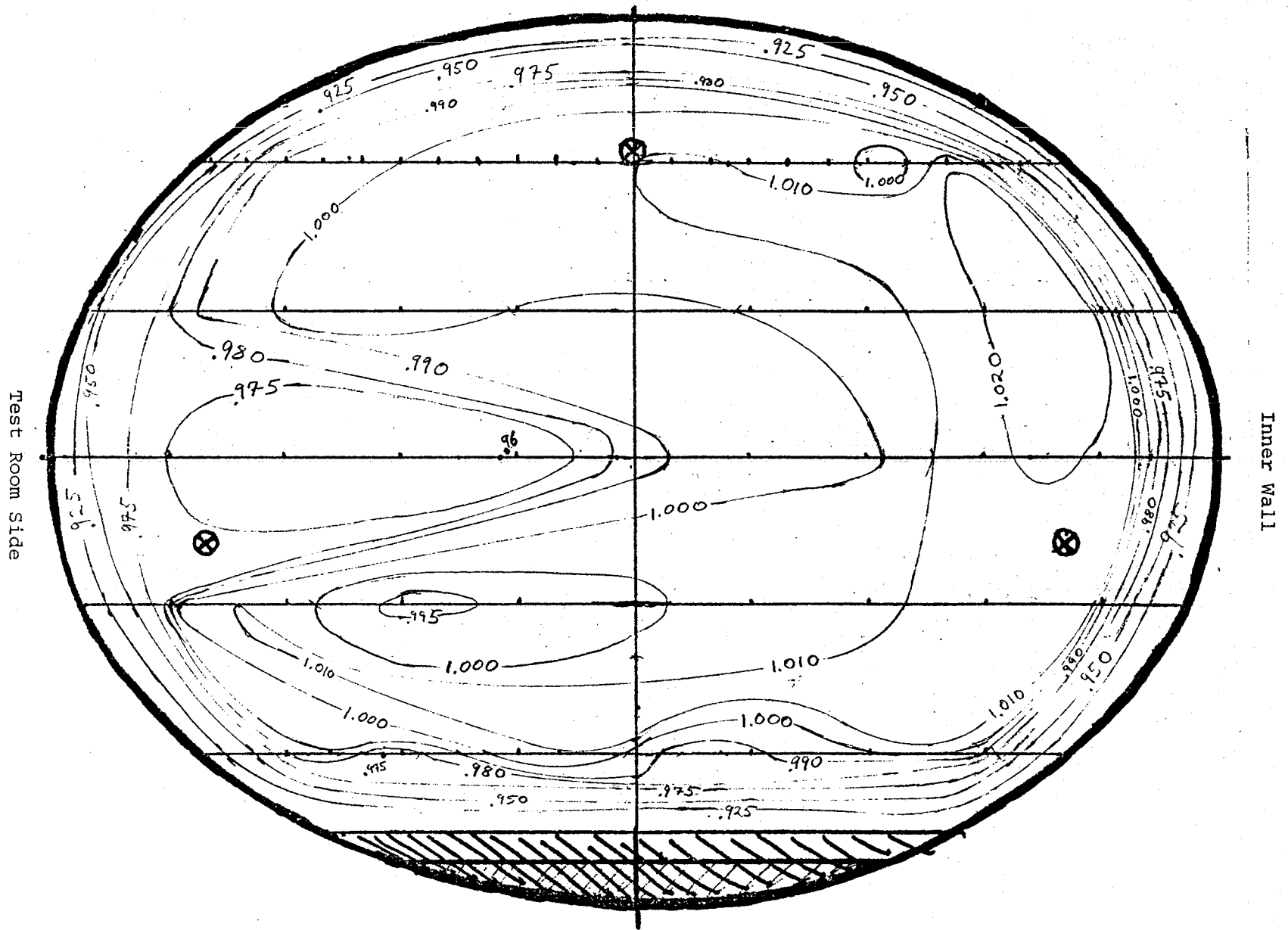


Appendix III, Part B (continued)
 Pressure coefficient distribution across tunnel section.
 Rake position 8.

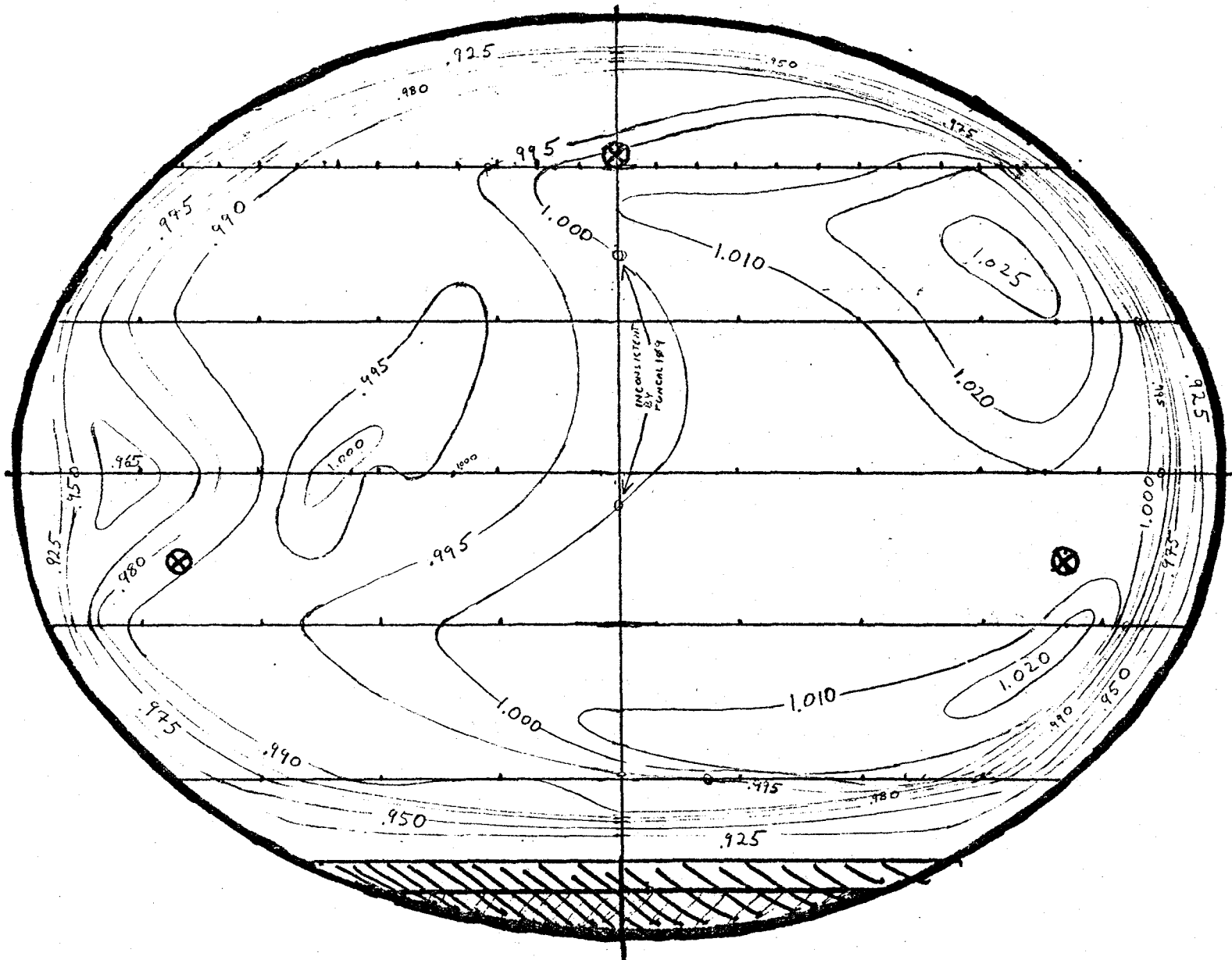
Pitot-static tube
causes interference



Appendix III, Part B (concluded)
Pressure coefficient distribution across tunnel section.
Rake position 9.

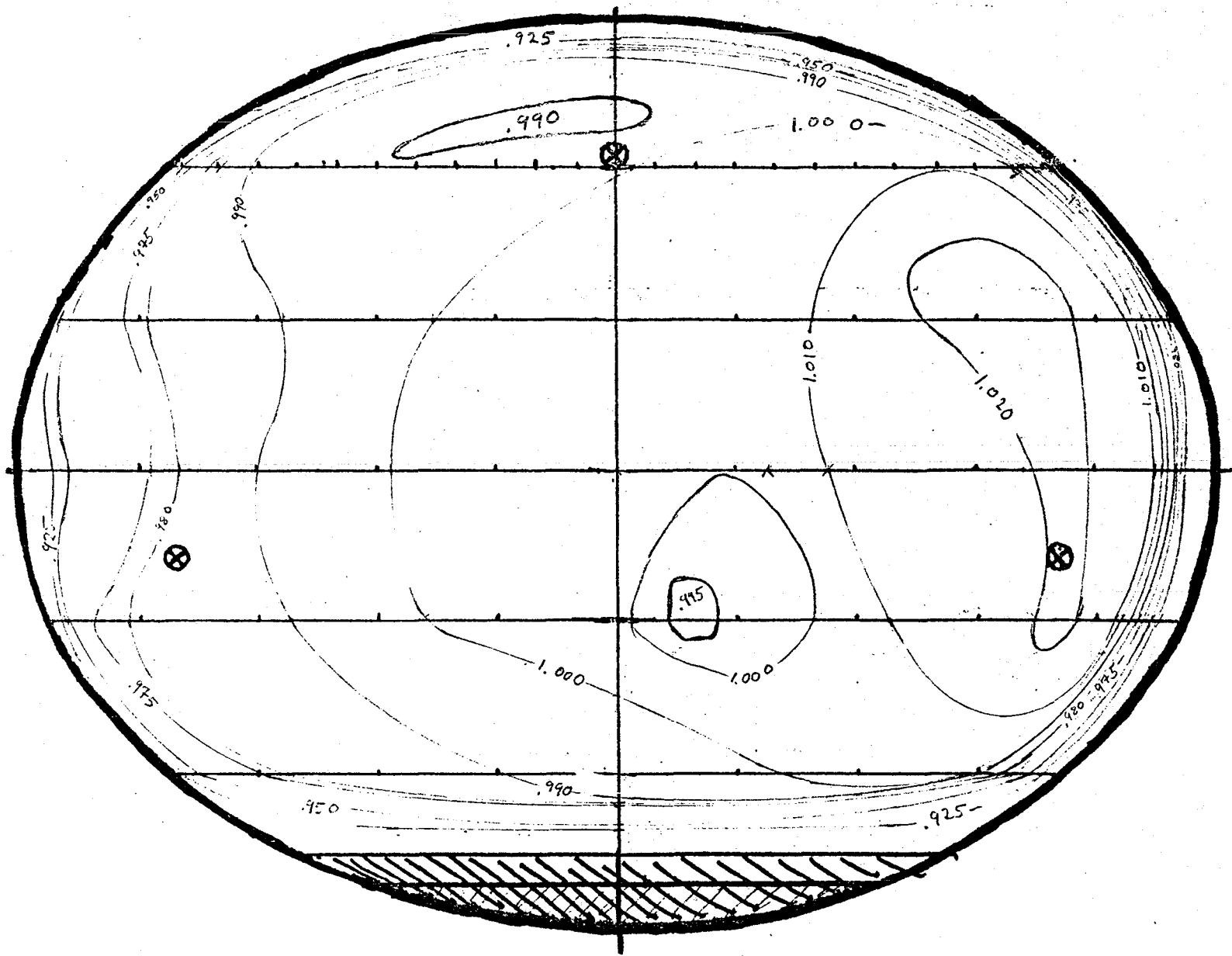


Appendix III, Part C: Contours of Constant Pressure Coefficient C_p
TUNCAL Phase of Test, Facing Upstream
Wind speed 35 mph

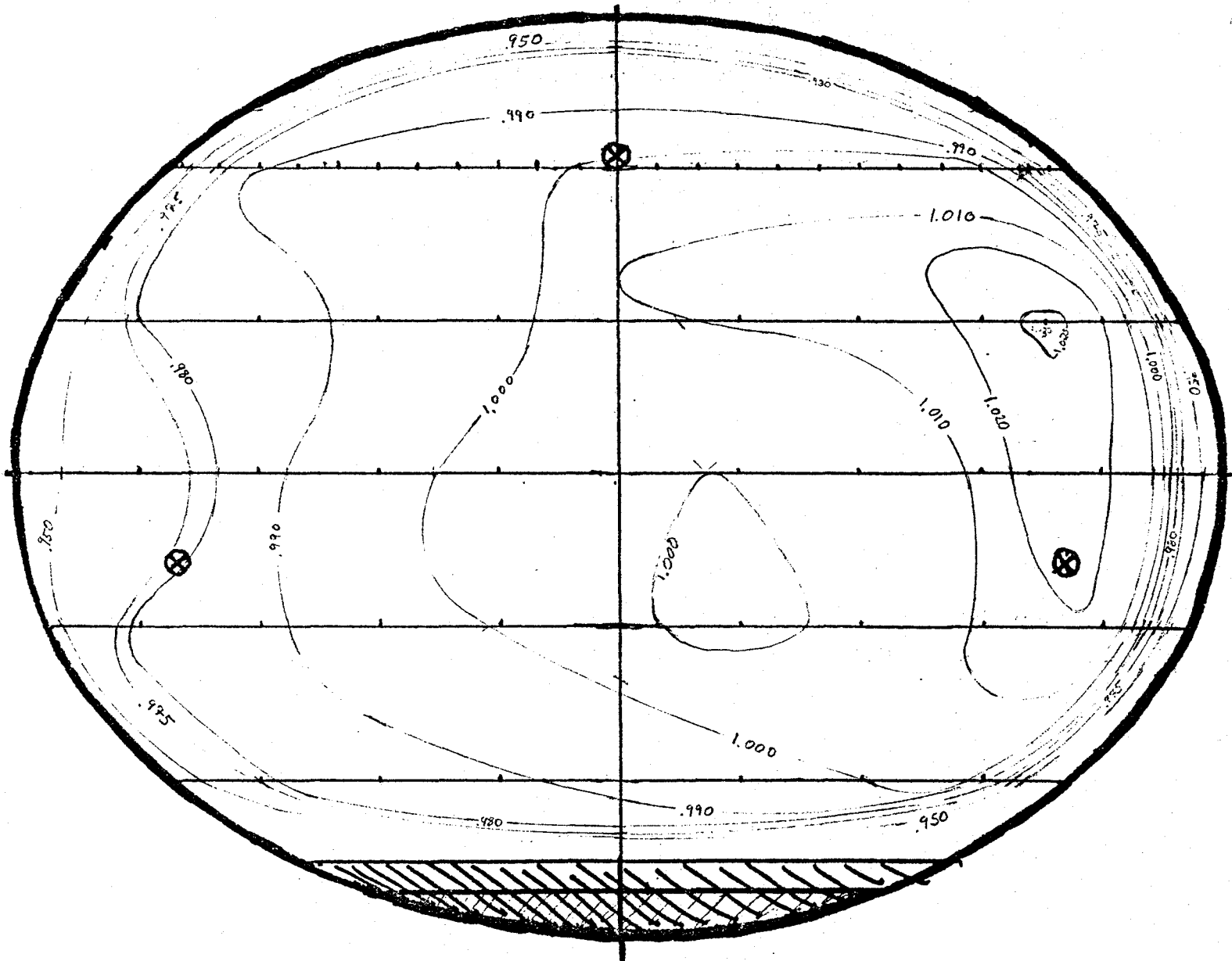


Appendix III, Part C.
(continued)

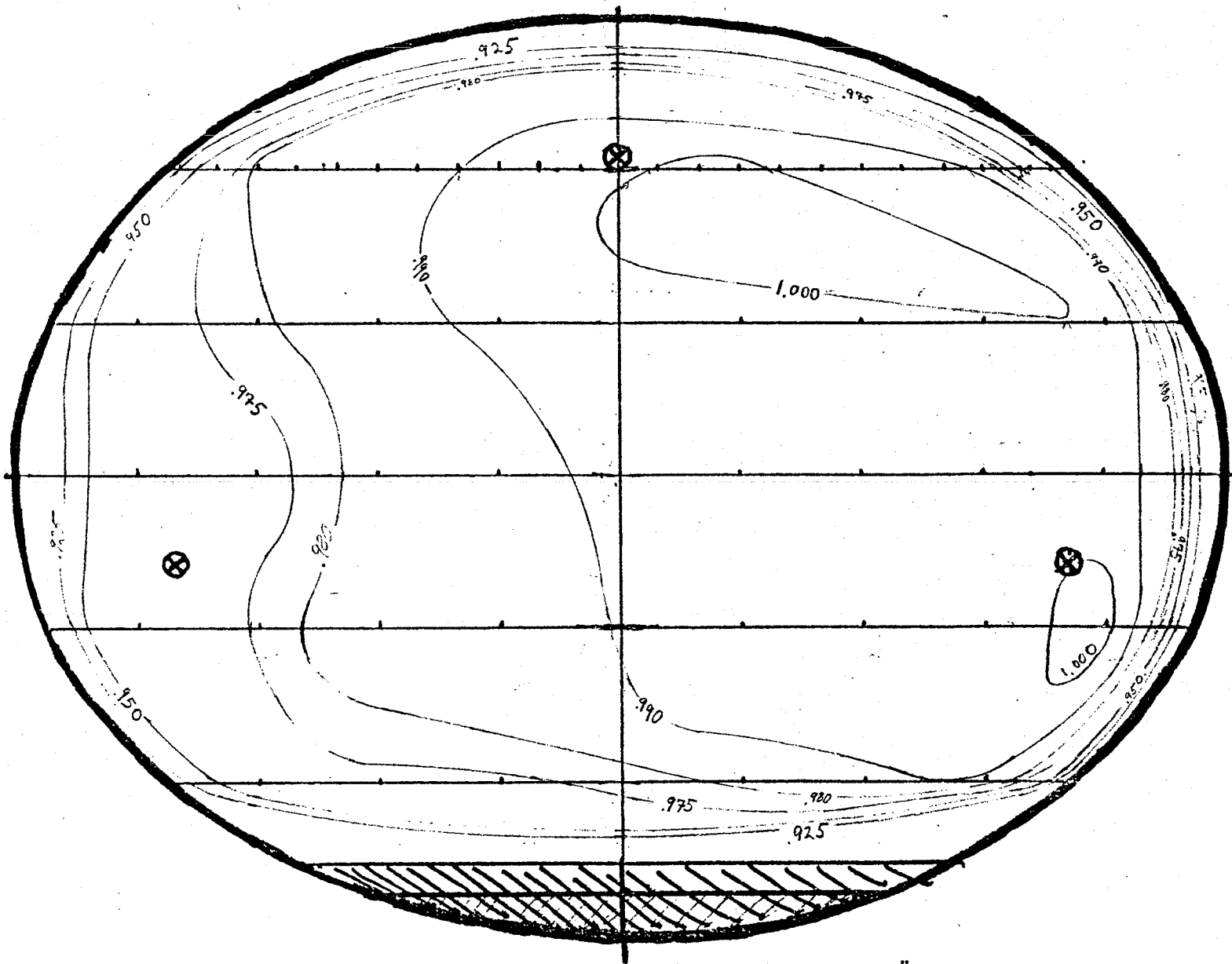
Contours of Constant Pressure Coefficient C_{p_n}
TUNCAL Phase of Test, Facing Upstream
Wind speed 50 mph



Appendix III, Part C. Contours of Constant Pressure Coefficient C_p _n
 (continued) TUNCAL Phase of Test, Facing Upstream
 Wind speed 70 mph



Appendix III, Part C. Contours of Constant Pressure Coefficient C_{p_n}
 (continued) TUNCAL Phase of Test, Facing Upstream
 Wind speed 100 mph



Appendix III, Part C. Contours of Constant Pressure Coefficient C_p "
 (concluded) TUNCAL Phase of Test, Facing Upstream
 Wind speed 125 mph

APPENDIX IV, Part A

Uncorrected Calibration Data for TUNCA2.abc Files, Second (Downstream) Plane

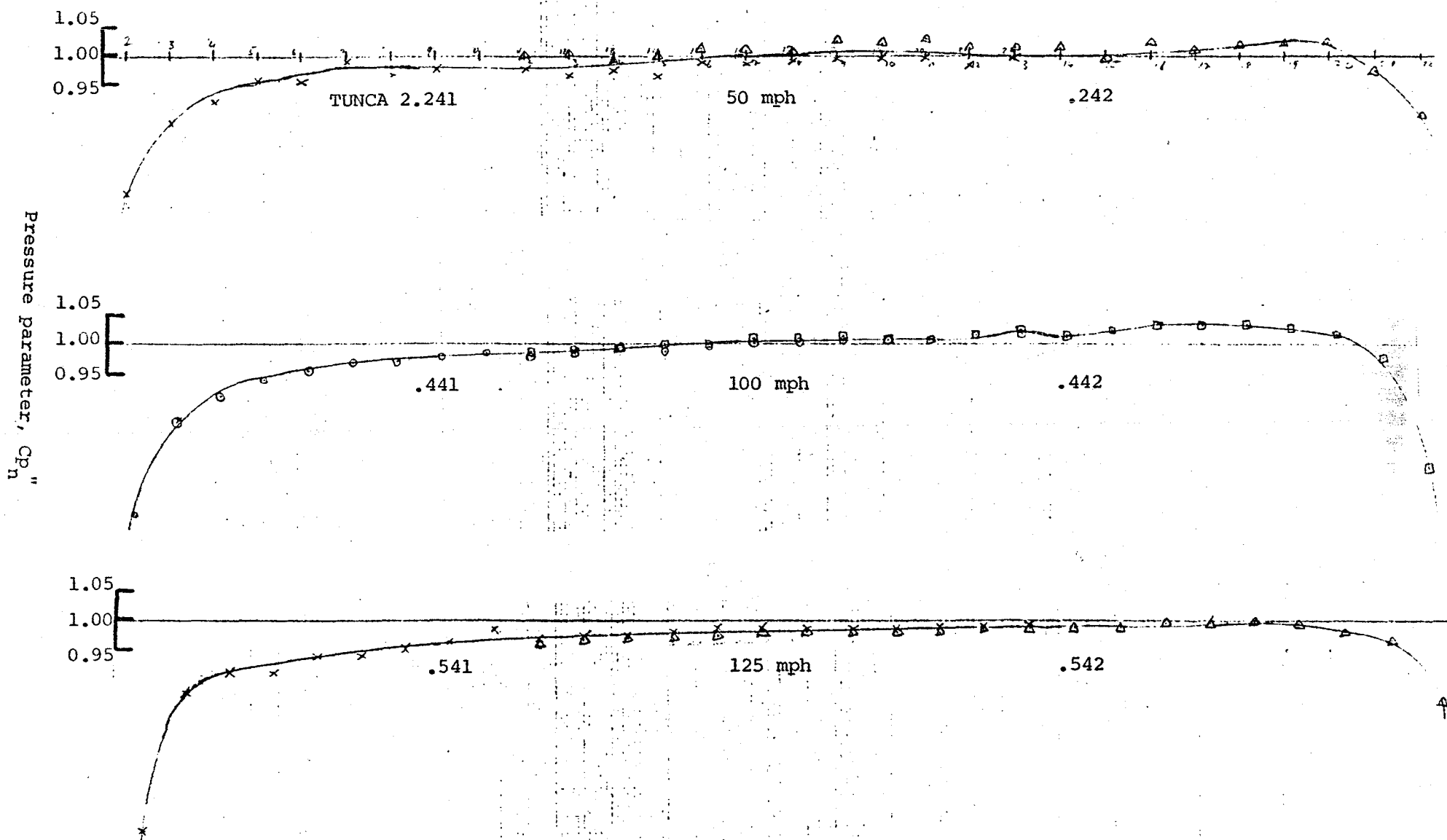
FILE.abc	.241	.242	.243	.245	.246	.247	.248	.441	.442	.443	.445	.446	.447
Vel.,mph	49.2	49.4	49.7	48.7	49.7	49.5	49.2	100.1	98.8	100.1	100.1	100.1	99.9
TAP	Cp _n												
1	1.009	1.005	1.011	1.015	0.995	1.009	1.005	1.008	1.008	0.999	1.001	1.003	1.003
2	0.885	1.004	0.939	0.931	0.901	1.017	0.932	0.854	0.998	0.904	0.949	0.854	0.992
3	0.949	1.006	0.998	0.990	0.960	1.003	0.973	0.938	0.997	0.967	0.967	0.969	0.994
4	0.966	0.999	1.004	0.994	0.975	1.016	0.987	0.960	1.004	0.971	0.975	0.976	0.998
5	0.987	1.001	1.003	0.985	0.979	1.007	0.990	0.974	1.005	0.980	0.978	0.985	1.000
6	0.983	1.007	1.007	0.990	0.984	1.013	0.995	0.982	1.004	0.978	0.976	0.982	1.006
7	1.002	1.004	1.002	0.993	0.986	1.009	0.995	0.989	1.010	0.978	0.970	0.987	1.001
8	0.988	1.000	1.006	0.989	0.982	1.010	0.989	0.992	1.010	0.980	0.975	0.987	1.010
9	0.995	1.012	1.010	0.992	0.986	1.007	0.992	0.996	1.011	0.985	0.978	0.991	1.009
10	0.557	1.007	1.002	0.993	0.986	1.000	0.987	0.998	1.008	0.989	0.987	0.992	1.009
11	0.994	1.011	1.012	0.994	0.985	1.000	0.993	0.995	1.009	0.992	0.987	0.994	1.013
12	0.987	1.001	1.012	0.991	0.981	1.006	0.985	1.002	1.012	0.996	0.989	0.994	1.015
13	0.992	1.001	1.008	0.995	0.981	1.002	0.991	1.003	1.016	0.995	0.989	1.000	1.016
14	0.987	1.000	1.017	0.985	0.992	0.993	1.003	1.000	1.011	0.994	0.990	1.000	1.015
15	0.999	0.990	1.015	0.992	1.006	0.993	1.004	1.003	1.015	0.994	0.984	1.005	1.016
16	0.997	1.002	1.008	0.986	0.662	1.002	0.998	1.006	1.021	0.995	0.991	1.009	1.018
17	1.000	0.995	1.010	0.997	0.629	1.004	0.993	1.008	1.020	0.993	0.987	0.920	1.020
18	1.001	0.997	1.013	0.999	0.717	1.003	0.998	1.009	1.020	0.996	0.996	0.918	1.021
19	1.001	0.999	1.010	1.007	0.792	1.000	0.996	1.009	1.017	0.995	0.996	0.953	1.020
20	1.002	0.999	1.009	1.008	0.853	1.001	1.001	1.010	1.008	0.993	0.997	0.971	1.017
21	0.994	0.972	1.006	0.979	0.899	0.980	0.986	1.013	0.993	0.997	0.977	0.991	1.016
22	1.000	0.933	1.006	0.905	0.928	0.907	0.991	1.015	0.893	0.996	0.924	0.998	0.959
23	-0.032	-0.049	-0.030	-0.043	-0.051	-0.047	0.012	-0.021	-0.025	-0.016	-0.018	-0.018	-0.020
24	0.994	0.979	0.995	0.989	0.962	0.988	0.994	1.008	1.000	0.992	0.998	0.997	1.007
25	0.977	0.956	0.972	0.966	0.931	0.959	0.960	0.974	0.969	0.962	0.964	0.960	0.971
26	-0.032	-0.058	-0.044	-0.064	-0.065	-0.060	-0.067	-0.025	-0.037	-0.034	-0.039	-0.039	-0.038
27	1.010	0.991	1.011	1.004	0.988	1.001	1.020	1.020	1.016	1.009	1.012	1.014	1.019
28	-0.018	-0.026	-0.021	-0.035	-0.042	-0.035	-0.036	-0.007	-0.003	-0.009	-0.007	-0.009	-0.007
48	-0.010	-0.027	-0.015	-0.029	-0.036	-0.027	-0.029	-0.003	-0.003	-0.004	-0.002	-0.003	-0.002

NOTE: Three-digit descriptor .abc in file identifications of form TUNCA2.abc
 Designate: rake position by last digit (c), tunnel speed by first digit (a)
 [1,2,3,4,5 nominally 35,50,70,100,140 mph]

APPENDIX IV, Part A (continued)

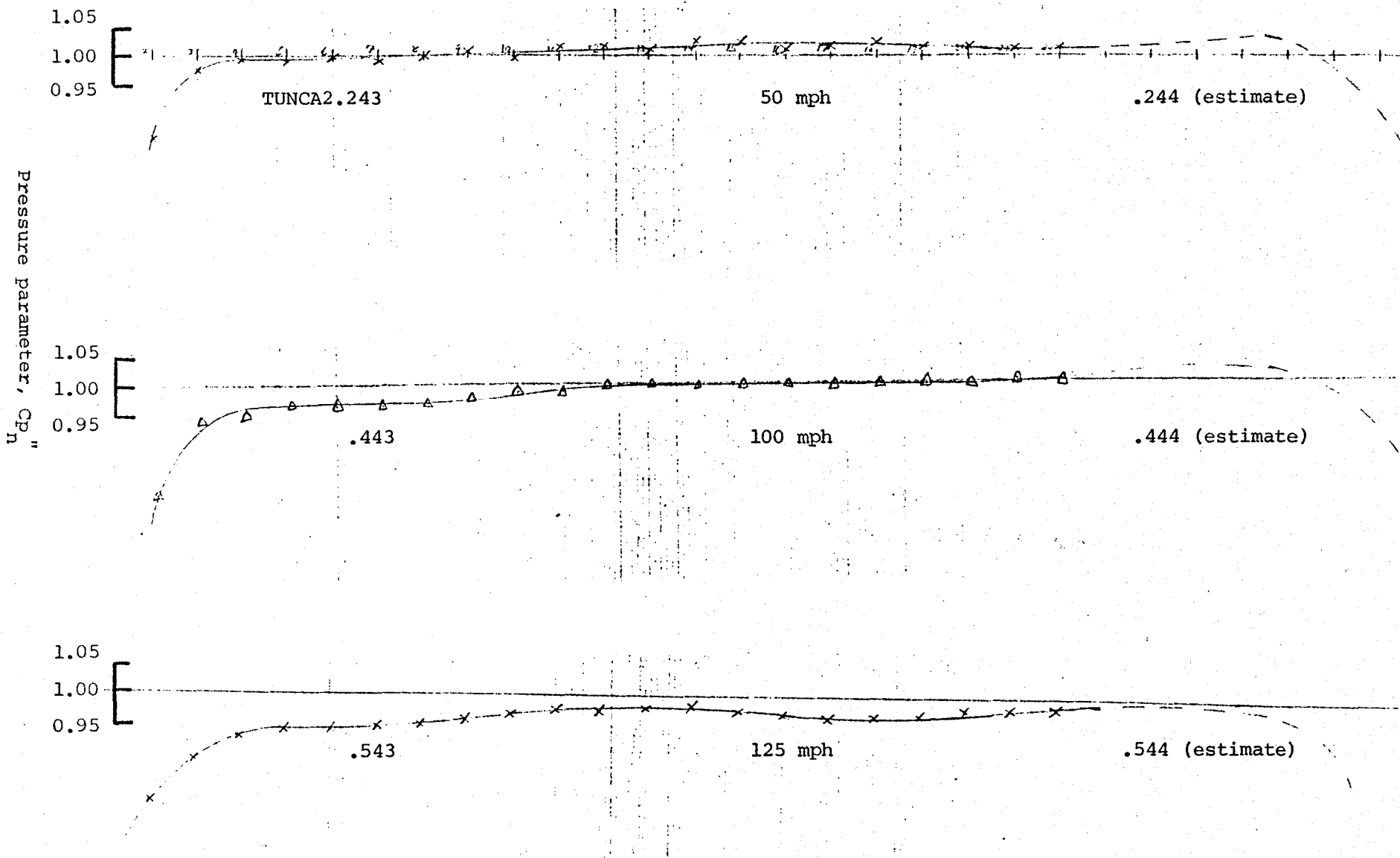
Uncorrected Calibration Data for TUNCA2.abc Files, Second (Downstream) Plane

FILE.abc	.448	.541	.542	.543	.545	.546	.547	.548
Vel.,mph	99.6	124.6	123.4	124.5	125.7	124.	122.8	123.7
TAP								
1	1.002	1.012	1.009	0.998	1.000	1.006	1.005	1.003
2	0.963	0.824	0.987	0.904	0.929	0.883	0.988	0.960
3	0.990	0.949	0.991	0.942	0.954	0.957	0.992	0.981
4	0.993	0.960	0.992	0.960	0.970	0.974	0.995	0.985
5	0.994	0.961	0.992	0.966	0.968	0.977	0.997	0.987
6	0.993	0.976	0.994	0.966	0.966	0.980	0.999	0.987
7	0.994	0.976	0.999	0.970	0.969	0.979	1.000	0.989
8	0.996	0.982	0.997	0.969	0.968	0.985	1.000	0.992
9	0.997	0.987	0.996	0.974	0.974	0.987	1.004	0.992
10	0.997	0.988	0.997	0.979	0.976	0.987	1.002	0.998
11	0.998	0.988	0.997	0.985	0.975	0.993	1.000	0.997
12	0.999	0.992	0.999	0.982	0.977	0.994	1.003	1.002
13	1.002	0.992	0.999	0.986	0.979	0.997	1.000	1.000
14	1.002	0.996	1.000	0.987	0.982	0.999	1.004	1.000
15	1.003	1.000	1.001	0.983	0.977	1.001	0.999	0.996
16	1.005	1.001	1.004	0.981	0.978	1.000	0.999	0.999
17	1.001	1.000	1.004	0.978	0.973	1.003	1.002	0.997
18	0.999	1.000	1.006	0.980	0.980	1.002	1.001	0.995
19	0.998	0.999	1.004	0.981	0.986	1.001	1.005	0.995
20	0.997	1.001	0.997	0.984	0.990	1.002	1.003	0.983
21	0.993	1.001	0.988	0.986	0.987	1.003	0.987	0.975
22	0.961	1.003	0.936	0.987	0.948	1.001	0.959	0.913
23	0.039	-0.012	-0.016	-0.008	-0.008	-0.009	-0.013	0.044
24	0.998	1.009	1.004	0.993	0.998	1.001	1.004	1.003
25	0.972	0.959	0.953	0.948	0.953	0.960	0.962	0.959
26	-0.041	-0.026	-0.037	-0.032	-0.041	-0.040	-0.036	-0.040
27	1.012	1.008	1.005	0.999	0.997	1.000	1.003	1.000
28	-0.009	-0.003	0.001	-0.004	-0.004	-0.006	-0.004	-0.006
48	-0.003	-0.002	-0.002	-0.002	-0.003	-0.002	-0.001	-0.002



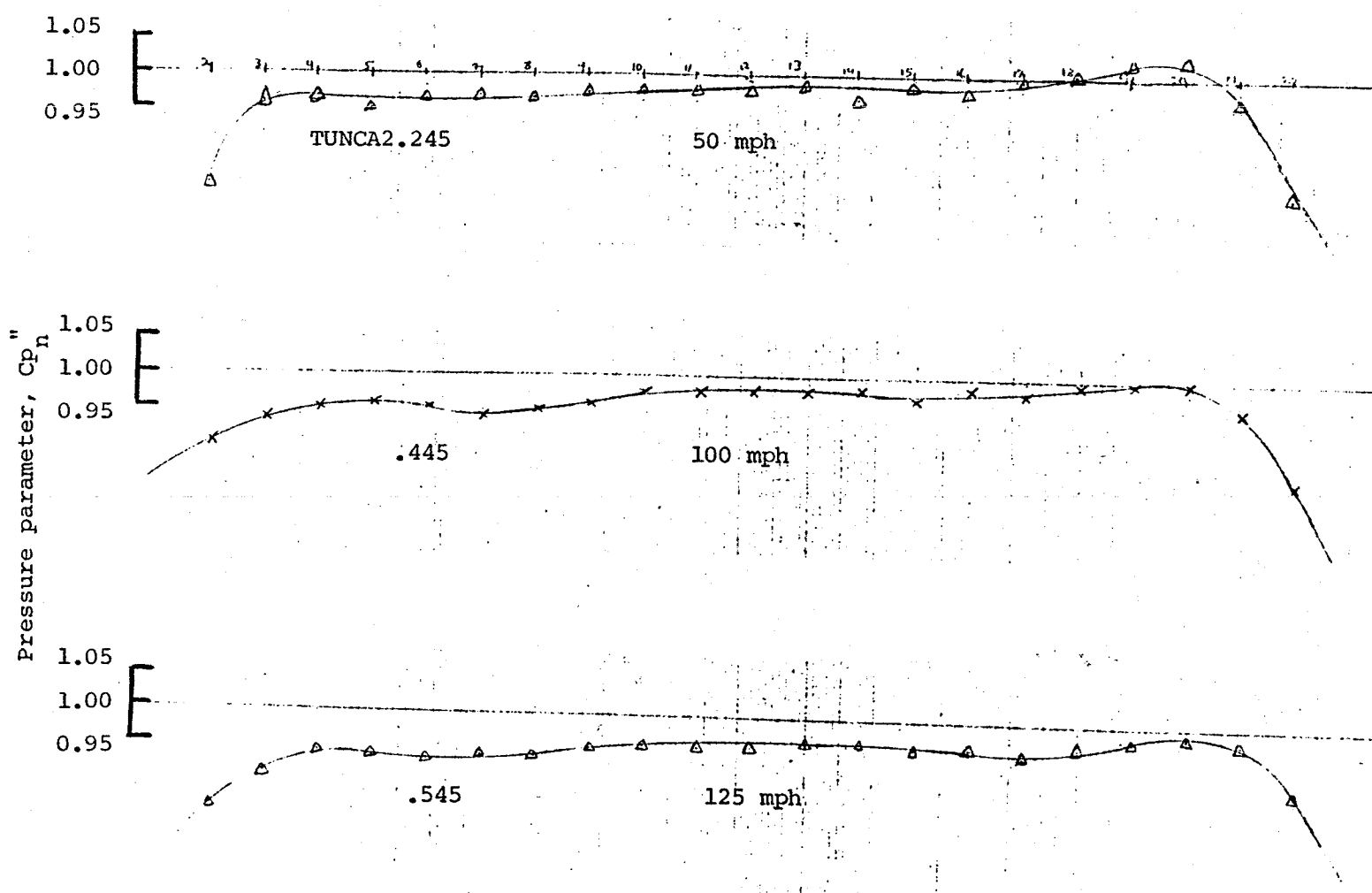
Appendix IV, Part B

Pressure coefficient distribution across tunnel section. Rake positions 1 and 2.

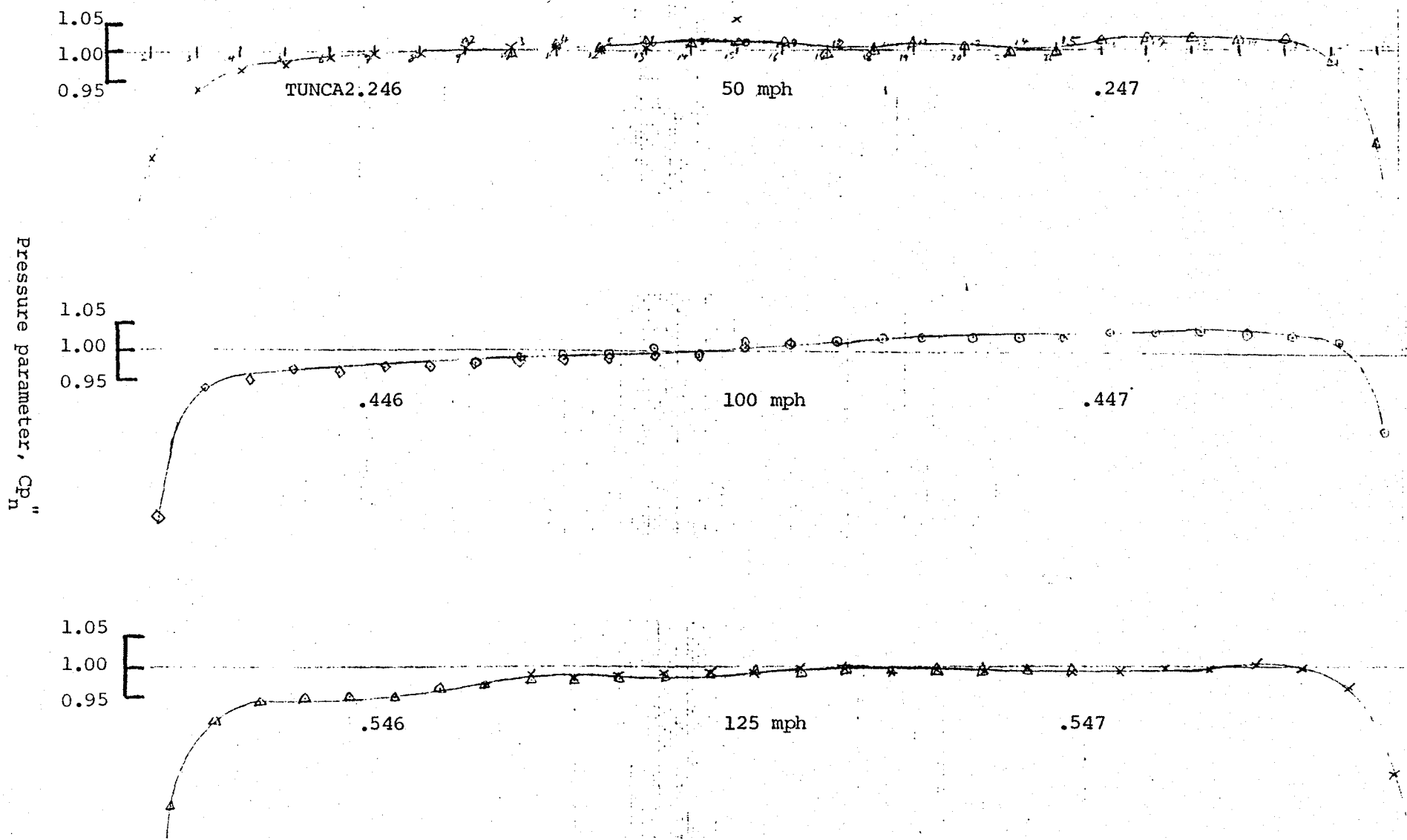


Appendix IV, Part B (continued)

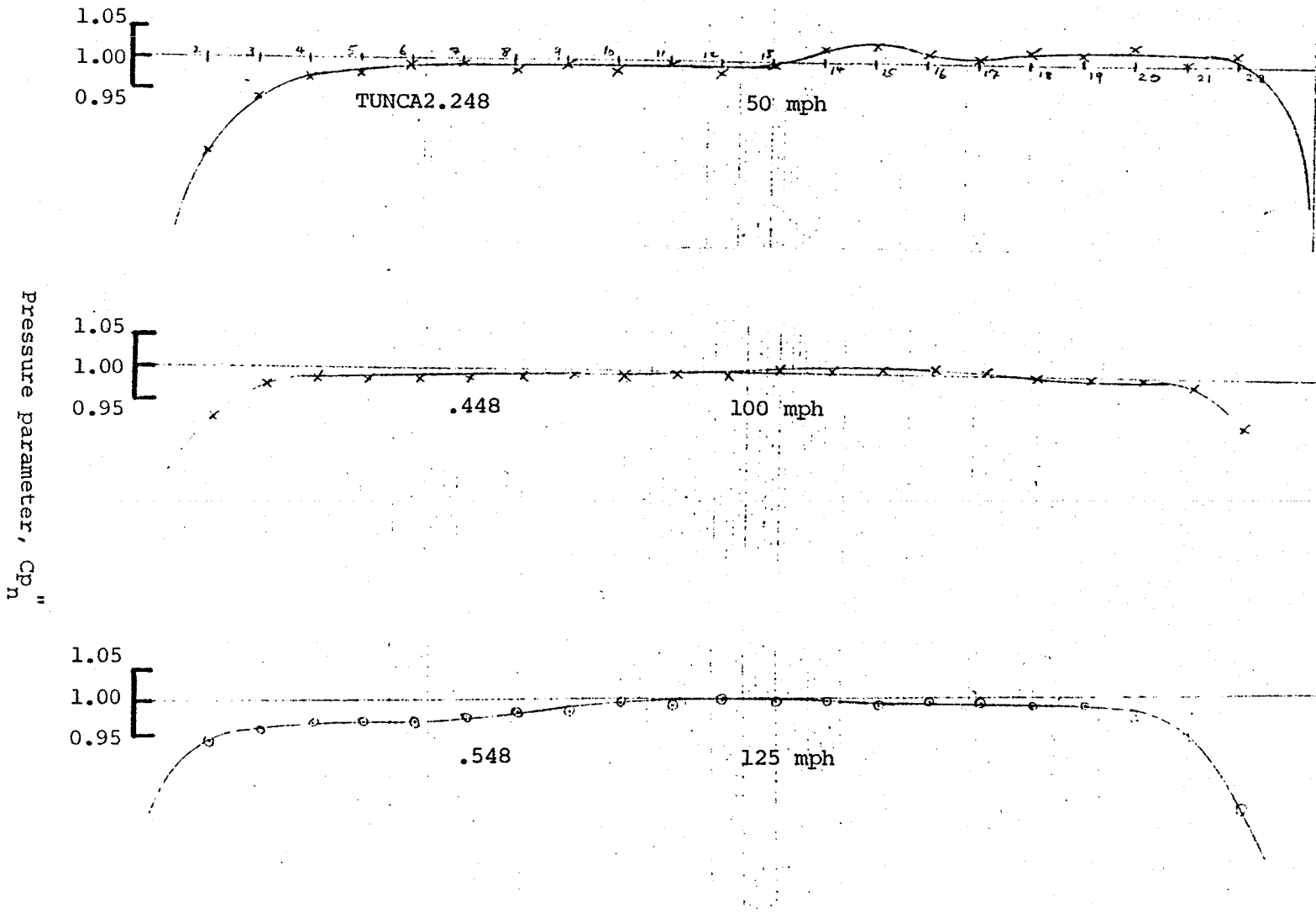
Pressure coefficient distribution across tunnel section. Rake positions 3 and 4 (estimated)



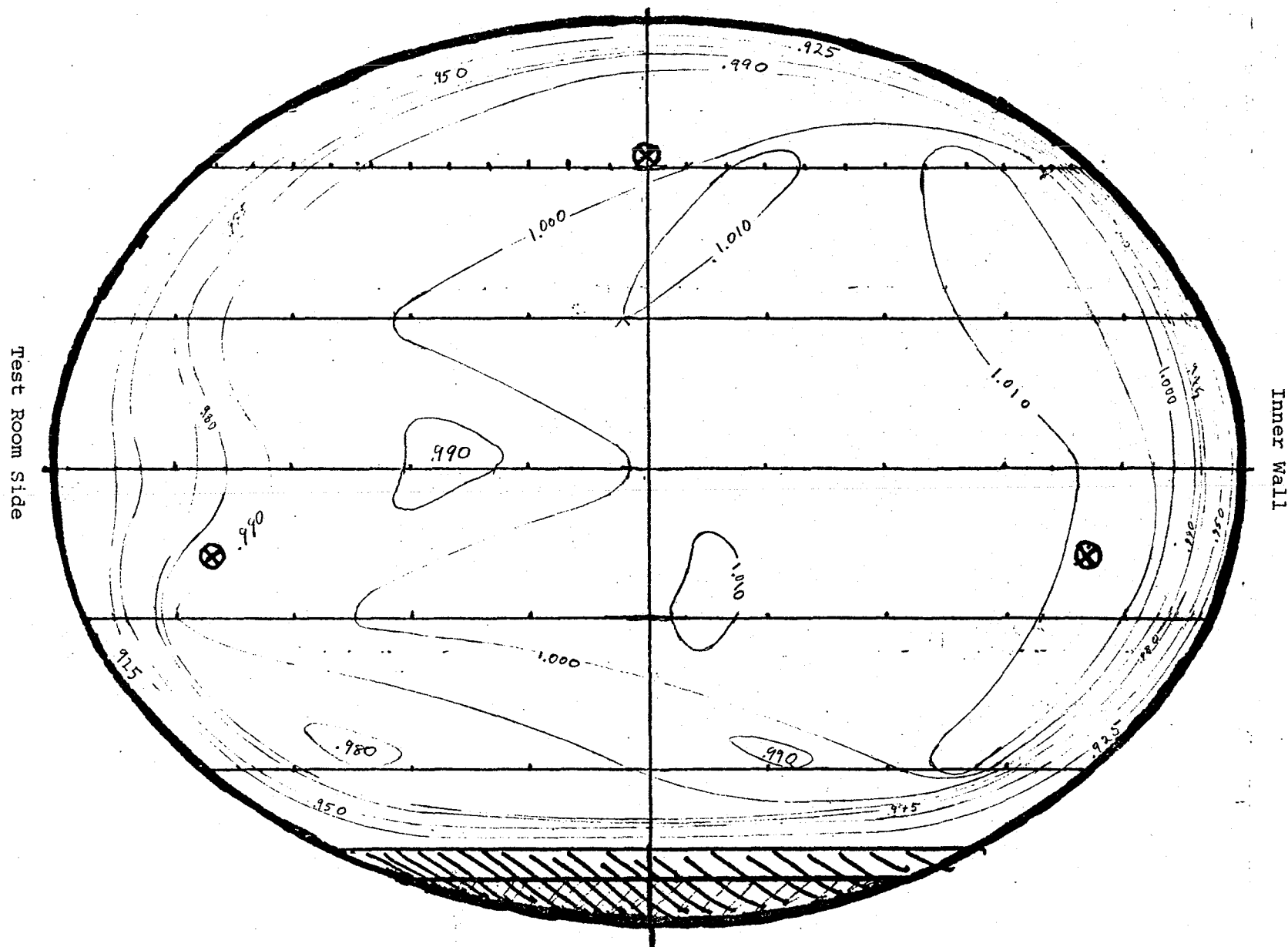
Appendix IV, Part B (continued)
 Pressure coefficient distribution across tunnel section. Rake position 5.



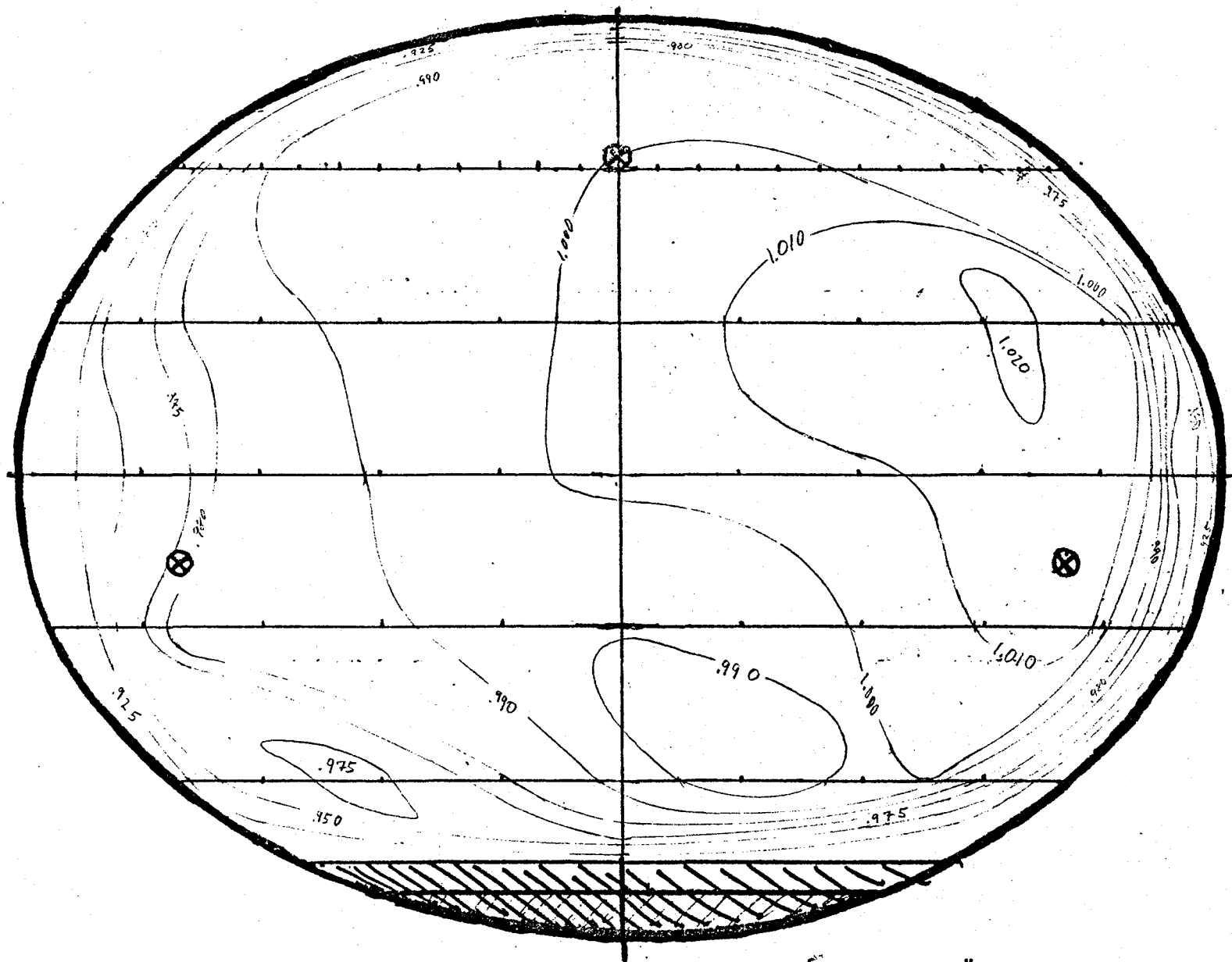
Appendix IV, Part B (continued)
 Pressure coefficient distribution across tunnel section. Rake positions 6 and 7.



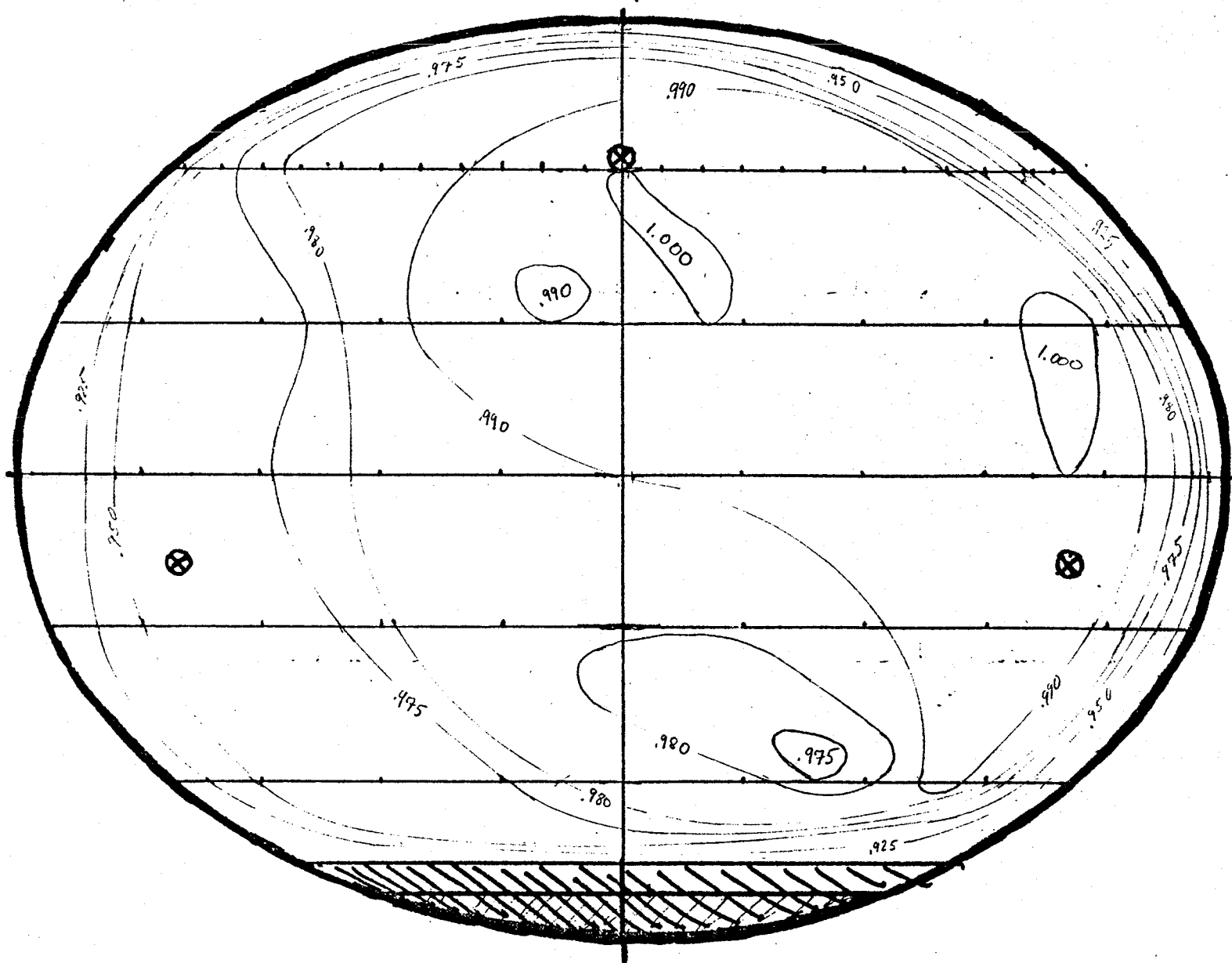
Appendix IV, Part B (concluded)
 Pressure coefficient distribution across tunnel section. Rake position 8.



Appendix IV, Part C. Contours of Constant Pressure Coefficient C_p "
 TUNCA2 Phase of Test, Facing Upstream
 Wind speed 50 mph



Appendix IV, Part C. Contours of Constant Pressure Coefficient C_p "
 (continued) TUNCA2 Phase of Test, Facing Upstream
 Wind speed 100 mph



Appendix IV, Part C. Contours of Constant Pressure Coefficient C_p "
 (concluded) TUNCA2 Phase of Test, Facing Upstream
 Wind speed 125 mph

Adaptation of Two-Dimensional
Transonic Analysis Code, TSFOIL, for
Use in Modeling Adaptive Wall
Test Sections

May 23, 1983

By: Jonathan Webb

Advisor: Prof. E.M. Murman

Introduction

A difficulty encountered when performing wind tunnel tests is determining how to correct for interference caused by the walls of the test section. While all wind tunnel testing encounters this difficulty, the effect of wall interference becomes most pronounced as the flow Mach number approaches unity. Shock waves forming on the aerodynamic surfaces propagate laterally instead of being swept downstream as in supersonic flow. This can choke the tunnel as in a convergent-divergent nozzle leading to gross errors in pressure as well as balance data. Numerous techniques have been developed over the years in an effort to combat this and other difficulties encountered with wind tunnel testing near Mach 1. Slotted or porous walls, correction parameters and enlarged test sections are among the most successful techniques but they are all fixes to a problem and are often dependent on engineering judgement when they are applied to an actual test.

A technique currently being developed by NASA at Langley Research Center is an adaptation of a technique originally developed in England in the 1940's. For a two dimensional test, if the top and the bottom walls of the test section can be deformed so they are the same shape as a free air streamline, all the effects of wall interference would be eliminated.

There are a number of difficulties with this approach. The principle difficulty is, once the proper streamline shape has been found, the wall will never correspond exactly to the shape of the streamline. It is hoped the elastic deformations

will be small enough so the wall held to a particular shape at only a few points will still reduce the interference considerably.

The purpose of this project is to simulate numerically the effects of the elastic deformation of the wind tunnel wall held to a streamline-like shape. The wall itself is simulated by a finite element model and is allowed to deform under the pressure loading developing in the wind tunnel with an airfoil model present. A modified version of the transonic analysis program, TSFOIL, is then used to determine the resulting flow field with the effects of the deformed wall included. The shape of the wall is updated during the course of the iterative solution of the flow field so the resulting solution correctly models the interaction between the shape of the wall and the flow field. Once a result from a particular operating condition has been obtained, the pressure distribution on the airfoil in the wind tunnel model can be compared with solutions generated with TSFOIL in free air mode. Any differences between the two solutions are primarily due to the interference effects of the deformed wall.

The Finite Element Model

The finite element model used to represent the wall is based on the principle of stationary, total potential energy (PSTPE) and the Rayleigh-Ritz procedure. Each segment of the wall between the jacks is treated as an individual element. A quintic, polynomial, bending only shape function is used to describe the deformation of the element. The von Karman plate formulation for the strain energy (see Reference 1) is used and is simplified by assuming the bending of the plate to be two dimensional. Use of the Rayleigh-Ritz procedure and the PSTPE result in a system of linear, algebraic equations which are solved by point relaxation. The resulting shape of the wall is then included in the flow field calculation.

For two dimensional, plate bending with no axial loading, the expression for the internal strain energy is:

$$u_b = \frac{1}{2} * \int D(w'')^2 dx \quad (1)$$

where:

u_b is the bending strain energy density per unit width

w is the bending deflection

' denotes differentiation with respect to the axial coordinate, x

$$D = \frac{E t^3}{12(1-\nu^2)}$$

E is Young's modulus = 2.8×10^7 psi

t is the plat thickness

ν is Poisson's ratio = 0.3

By equating the strain energy to the work done on the element by the externally applied loads, the PSTPE can be applied and the unknown constants in the shape function can be found.

The work done by the externally applied loads is given by:

$$u_e = - \int p_z * w dx \quad (2)$$

where:

u_e is the external work density per unit width

p_z is the applied load per unit area in the bending direction

The Rayleigh-Ritz procedure uses an assumed function which will describe the displacements of the element. For this model, a quintic polynomial shape function is used. This shape is:

$$w = a_1 + a_2x + a_3x^2 + a_4x^3 + a_5x^4 + a_6x^5 \quad (3)$$

where the a_n 's are unknown constants to be determined.

It is desirable to describe the deformation of the element in terms of displacement quantities which are defined at the ends of the element. These generalized displacements are described in Figure 1.

The generalized displacements (q's) can be found in terms of the coefficients of the shape function by using the following transformation.

$$(a_n) = J (q_n) \quad (4)$$

where:

(a_n) and (q_n) are column matrices of q_n and a_n

$$J = \begin{matrix} 1 & 0 & 0 & 0 & 0 & 0 \\ 0 & 1 & 0 & 0 & 0 & 0 \\ 0 & 0 & 1 & 0 & 0 & 0 \\ \frac{-10}{1^3} & \frac{-6}{1^2} & \frac{-3}{21} & \frac{10}{1^3} & \frac{-4}{1^2} & \frac{1}{21} \\ \frac{15}{1^4} & \frac{8}{1^3} & \frac{3}{21^2} & \frac{-15}{1^4} & \frac{7}{1^3} & \frac{-1}{1^2} \\ \frac{-6}{1^5} & \frac{-3}{1^4} & \frac{-1}{21^3} & \frac{6}{1^5} & \frac{-3}{1^4} & \frac{1}{21^3} \end{matrix}$$

If the shape function written in terms of the generalized displacements (using eq. 4) is introduced into the expression for the strain energy, the following expression results.

$$u_b = \frac{1}{2} \int D (a_n)^T (x^n) (x^n)^T (a_n) dx$$

The integral can be evaluated to give:

$$\begin{array}{cccccc}
 E^* = & 0 & 0 & 0 & 0 & 0 & 0 \\
 & 0 & 0 & 0 & 0 & 0 & 0 \\
 & 0 & 0 & 4l & 6l^2 & 8l^3 & 10l^4 \\
 & 0 & 0 & 6l^2 & 12l^3 & 18l^4 & 24l^5 \\
 & 0 & 0 & 8l^3 & 18l^4 & \frac{144l^5}{5} & 40l^6 \\
 & 0 & 0 & 10l^4 & 24l^5 & 40l^6 & \frac{400l^7}{7}
 \end{array} \quad (5)$$

where l is the length of the segment.

The transformation given by eq. 4 and the element stiffness matrix defined as:

$$K = D J^T E^* J \quad (6)$$

where:

$$\frac{K}{D} = \begin{array}{cccccc}
 \frac{120}{7l^3} & \frac{60}{7l^2} & \frac{3}{7l} & \frac{-120}{7l^3} & \frac{60}{7l^2} & \frac{-3}{7l} \\
 \frac{60}{7l^2} & \frac{192}{35l} & \frac{-24}{35} & \frac{-60}{7l^2} & \frac{108}{35l} & \frac{-4}{35} \\
 \frac{3}{7l} & \frac{-24}{35} & \frac{76l}{70} & \frac{-3}{7l} & \frac{39}{35} & \frac{1}{70} \\
 \frac{-120}{7l^3} & \frac{-60}{7l^2} & \frac{-3}{7l} & \frac{120}{7l^3} & \frac{-60}{7l^2} & \frac{3}{7l} \\
 \frac{60}{7l^2} & \frac{108}{35l} & \frac{39}{35} & \frac{-60}{7l^2} & \frac{192}{35l} & \frac{-11}{7} \\
 \frac{-3}{7l} & \frac{-4}{35} & \frac{1}{70} & \frac{3}{7l} & \frac{-11}{7} & \frac{31}{35}
 \end{array}$$

The generalized displacements can be introduced into the expression for the external work and used to find the generalized loads. Defining the displacement, w , in terms of the generalized displacements yields:

$$w = (D^*)^T (q_n) \quad (7)$$

where:

$$\begin{aligned} (D^*) = & 1 - 10(x/l)^3 + 15(x/l)^4 - 6(x/l)^5 \\ & x - 61(x/l)^3 + 81(x/l)^4 - 31(x/l)^5 \\ & x^2 - 31^2(x/l)^3 + 1.51^2(x/l)^4 - \frac{1}{2}1^2(x/l)^5 \\ & 10(x/l)^3 - 15(x/l)^4 + 6(x/l)^5 \\ & -41(x/l)^3 + 71(x/l)^4 - 31(x/l)^5 \\ & \frac{1}{2}1^2(x/l)^3 - 1^2(x/l)^4 + \frac{1}{2}1^2(x/l)^5 \end{aligned}$$

Introducing these expressions into the integral for the external work gives:

$$u_e = - \int p_z (D^*)^T (q_n) dx$$

or

$$u_e = - (q_n)^T (Q) \quad (8)$$

where

$$(Q) = \int p_z (D^*) dx \quad (9)$$

Applying the PSTPE to the individual element yields:

$$K (q_n) = (Q) \quad (10)$$

These expressions are only valid for an individual element. To model the entire wall, an assemblage of these elements is required. By equating certain displacement quantities at junctions between elements, a single expression of the same form as eq. 10, valid for the entire wall, can be determined. For the quintic shape function used, w' and w'' are required to be continuous at the element junctions. This is the same as requiring:

$$q_5^n = q_2^{n+1}$$

and

$$q_6^n = q_3^{n+1}$$

where the superscript n is the number of the individual element.

The generalized loads must be assembled in a somewhat different way. The load associated with q_2 , q_3 , q_5 or q_6 must be added to the load from the adjoining element identified by the equalities above.

To complete the assemblage of the local elements, the boundary conditions must be included in the global equations. At the upstream end of the wall, w' is set to 0. At the downstream end of the wall, w'' is set to 0. Since the

element junctions are also the jack locations, w is prescribed at each node. Elements of the global stiffness matrix corresponding to the generalized displacements known from the boundary conditions are removed. Known elements effecting unknown displacements are included in the terms for the global generalized loads. This is so the only components of the global stiffness matrix remaining are those associated with the unknown, generalized displacements.

Once the global equation has been determined, the resulting system of linear, algebraic equations is inverted using point, successive, over relaxation. This is not a method normally used for solving this type of system but an S.O.R. subroutine was readily available and could be used with very little modification. Reference 2 outlines the general procedure used.

Once the generalized displacements have been determined from the relaxation procedure, the deformation of the wall can be easily found using the J transformation matrix given by eq. 4. Wall displacements are determined at mesh points used during the current iteration in TSFOIL and the slopes of the wall at those mesh points is determined by using the cubic spline subroutine included in TSFOIL. The wall slopes are then used to modify the wall boundary condition and the flow field calculation proceeds.

Modifications to TSFOIL

The transonic, two dimensional, small disturbance analysis program, TSFOIL, written by Earll Murman, Frank Bailey and Margaret Johnson and documented by Stephen Stahara in NASA CR-3064, was modified for use in this study. The modifications allowed the use of a variable geometry wall when specifying the boundary conditions with the shape of the wall predetermined. The downstream boundary condition was also modified to better simulate the test section being modeled.

In the original version of the program, a zero gradient condition was used at the downstream boundary of the computational domain. In the version used for this study, the downstream condition was based on the one dimensional, isentropic, gas flow relation:

$$\frac{du}{u} = \frac{-dA}{A} * \frac{1}{1-M^2} \quad (11)$$

where:

u is the exit flow velocity

A is the exit cross sectional area

M is the exit Mach number

Equation 11 can be differentiated with respect to the axial coordinate, x, and, upon introducing the perturbation velocity potential, can be written as:

$$\frac{\phi''}{u} = \frac{-dA}{dx} * \frac{1}{A(1-M^2)} \quad (12)$$

This expression can be written in difference form for a non-uniform mesh as:

$$\begin{aligned} \phi_{i+1} = & \frac{1}{2}(x_{i+1} - x_{i-1}) (x_{i+1} - x_i) * B \\ & + \frac{x_{i+1} - x_i}{x_i - x_{i-1}} (\phi_i - \phi_{i-1}) + \phi_i \end{aligned} \quad (13)$$

where $B = \frac{-dA}{dx} * \frac{1}{A(1-M^2)}$

Equation 13 is used as an extrapolation formula at the downstream edge of the computational mesh.

The other modification to the boundary conditions involved the treatment of the walls of the test section. The original version of the program allowed only straight walled test sections to be modeled. For a wall with non-zero slope, the boundary condition must become:

$$\frac{d\phi}{dy} = \frac{dy}{dx} \quad (14)$$

where $\frac{dy}{dx}$ is the slope of the wall.

Since it is generally sufficient to include the boundary conditions to first order, eq. 14 can be written in finite difference form as:

$$\phi_w = (y_{w+1} - y_w) \frac{dy}{dx} + \phi_{w+1} \quad (15)$$

where the w subscript is the index at the wall. This form is used for the upper wall. For the lower wall, the direction of indexing is reversed.

Equation 15 is used as an extrapolation formula in the same manner as eq. 13 was used.

It was also necessary to modify a number of the subroutines in TSFOIL to interface the wall calculation with the flow field solution during the iteration process. The following is a list of the subroutines modified and a brief description of the modifications made to each.

TSFOIL was modified to call the subroutines generating the global stiffness matrix for the wall deformation analysis. The subroutine which generates the wall shape during a free air calculation is also called by TSFOIL.

READIN was modified to include the new input parameters in the new MIT/JCF VAX namelist statements.

BLOCKDATA was modified to include all of the new common blocks as well as default values for the input variables.

RESET was modified to include the boundary condition modifications described above. The vortex-doublet solution for the far field boundary was also removed from this subroutine. Since the computational mesh had to be extended to include the entire variable geometry wall, it was decided this portion of TSFOIL's original form would not be needed.

Since this flow field condition interacts with the program in many ways, it is not known how removing this section effects the remainder of the program.

FARFLD was modified to treat the variable geometry wall far field condition the same as the solid wall case of the original program.

SOLVE was modified to call the wall deformation routine.

The following are new subroutines added for this study:

STIFFMAT generates the global stiffness matrix for the structural solution. It calls subroutine KLOCAL which calculates the elements of the local element stiffness matrix needed for the global matrix.

WALLV is the controlling program for the deformation routine. It determines the pressure distribution along the wall from the perturbation velocity distribution, it calls the deformation routine and it determines the correctly scaled wall slopes to be used in the wall boundary condition.

DEFORM is the structural deformation analysis. This subroutine determines the global, generalized loads from the pressure distribution along the wall and the local wall geometry. Functions Q and BC determine the distribution factors for the pressure loads and the geometric boundary conditions respectively. The relaxation subroutine (subroutine RELAX) is also called from this subroutine. When the generalized displacements have been determined, DEFORM also determines the actual wall shape so subroutine WALLV

can determine the wall slopes as needed for the boundary conditions.

STREAM is the subroutine used to generate the streamline shape at the height of the tunnel walls. It is activated at the end of a free air case and can be used to generate the streamline shape internally for the wall deformation routine.

Progress to Date

In the original formulation of the deformation solution, a simplified form of the equilibrium plate equation was solved over segments of the wall in a manner similar to the finite element solution described previously. This method also led to a system of linear, algebraic equations for a set of unknown coefficients in a polynomial describing the deflection of the wall. This method was coded but a solution was never obtained from this procedure. It is not known whether the resulting system of equations was numerically ill-conditioned or if there were still undetected code errors.

The finite element procedure was introduced when no further progress was being made with the equilibrium method. The finite element method has not yielded a solution either; however, progress was still being made when work was stopped.

The boundary conditions for the variable wall shape have been tested by using the streamline input to WALLV but bypassing the deformation analysis in DEFORM. The relaxation solution seems to progress properly in TSFOIL but the results from the test case used have not been examined in detail nor have numerous test cases been run.

All of the cases for the variable wall geometry encounter fatal run-time errors in subroutine PRTWAL. The version being used in this study had been modified for a previous project and the error seems to be connected with those modifications. I do not believe using the original version of PRTWAL would alleviate the problem.

New Input Parameters

BCTYPE Integer. Set to 7 to activate the variable geometry wall solution.

SLINEU Real. Height of the wall from the centerline
SLINEL of the test section. Heights are positive for the upper wall and negative for the lower wall. Input one value for each point in the input mesh in order from upstream to downstream. Normalized to nominal 6" airfoil chord. Default: 1.1 and -1.1

*** Note *** If a free air case is run with STREAMGEN = .TRUE. , when allowed to run to the fine mesh, subroutine STREAM will automatically set up this data if the variable geometry wall is run without terminating the program between cases.

FREETEMP Free stream static temperature and pressure.
FREEPRES Must be input in degrees Rankine and psf.
Default: standard temperature and pressure.

NWALL Integer. Number of flow field iteration performed before the wall shape is updated.
Default: 10

WALLEND Logical. If .TRUE., the downstream end of the wall is set by the streamline input. If .FALSE., the last jack setting is set to the opening height given in the blueprints for the wall. Default: .TRUE.

STREAMGEN Logical. If .TRUE., a streamline is generated starting at +H and -H as defined by input. Default: .FALSE.

WALLDEF Logical. If .TRUE., the wall deformation analysis is called during a variable geometry wall case. Default: .TRUE.

References

- 1) Rivello, Analysis of Flight Structures
Chapter 13
- 2) Noble and Daniel, Applied Linear Algebra
Chapter 9
- 3) Stahara, Operational Manual For Two-Dimensional,
Transonic Code, TSFOIL; NASA CR-3064

**CALCULATING C-GRIDS
WITH FINE AND EMBEDDED
MESH REGIONS**

By
Bernard Loyd

CFDL-TR-83-7

December 1983

This research was performed in the Computational Fluid Dynamics Laboratory, M.I.T., and was supported under NASA Grant NAG1-206.

Department of Aeronautics and Astronautics
Massachusetts Institute of Technology
Cambridge, Massachusetts 02139

Table of Contents

Introduction and Summary	1
1. Technical Background	2
1.1 Fine Mesh Regions	4
1.2 Embedded Grids	6
2. Program Capabilities	9
3. Program Structure	10
4. Conclusions	11
5. References	12

Introduction and Summary

This report describes a program for calculating a C-type mesh around airfoil like shapes. The Jameson/Caughey approach is used: a parabolic transformation coupled with a shearing transformation. The algebraic algorithm is capable of efficiently generating nearly orthogonal grids.

A high degree of grid control is possible. The user may specify grid boundaries, number of grid lines, and location of (and spacing in) trailing edge and leading edge fine mesh areas. The capability of embedding fine mesh regions, for use with new adaptive grid techniques, is being developed.

Grids generated by the program have been used in Euler flow calculations by W. Usab [5]. Results superior to results calculated on previous O-type grids were obtained. Specifically, calculations converged faster using C-grids rather than O-grids, total pressure loss spikes at the trailing edge of the airfoil were eliminated, and the Ni method converged with zero artificial smoothing for a subcritical case (resulting overall total pressure loss was then nearly zero). These improvements were attributed to higher grid orthogonality, especially at the trailing edge.

This report is meant to serve as an outline of the C-mesh generator algorithm and its use. The program itself, is fairly straightforward. Roughly half of the 800 code lines are comment lines.

1. Technical Background

This discussion follows closely that found in [2]. Consider the physical space to be described in Cartesian coordinates, where x and y represent the streamwise and vertical coordinates respectively. We introduce a singular point just inside the leading edge of the airfoil. This singular point will be the locus of branch points in subsequent transformations that unwrap the airfoil to a shallow bump. The location is chosen to make the bump as smooth as possible.¹ We represent the singular line as:

$$\bar{x} = x_s,$$

$$\bar{y} = y_s$$

and define

$$x = \bar{x} - x_s$$

$$y = \bar{y} - y_s$$

We then introduce the conformal mapping

$$X_1 + Y_1 = (x + y)^{1/2}$$

which, after equating real and imaginary parts gives us two families of orthogonal parabolas,

$$X_1 - Y_1 = x$$

and

$$2X_1 * Y_1 = y.$$

This transformation maps the entire airfoil to a shallow bump near $Y_1 = 0$ (see Fig. 1).

¹If the nose of the airfoil can be represented by a parabola, the optimal branch point is the focal point. Otherwise, trying several values of x_s close to .005(chord) has quickly given an optimum for the geometries tested to date.

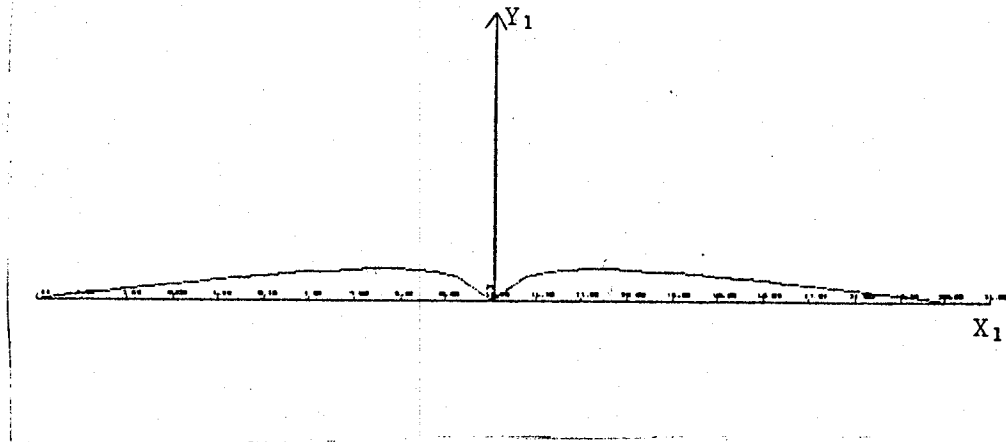


Fig 1a. Conformal Transformation with $(x_s, y_s) = (0, 0)$.

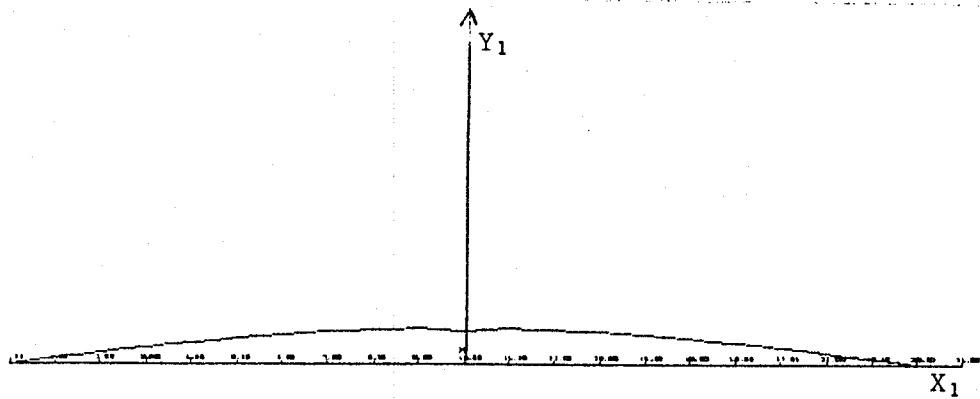


Fig 1b. Conformal Transformation with $(x_s, y_s) = (0.006, 0)$.

Figure 1.

(Absolute values of Y_1 are used to allow more accurate spline fit.)

Defining the height of this bump as

$$Y_1 = S(X_1)$$

the final shearing transformation,

$$\xi = X_1$$

$$\eta = Y_1 - S(X_1)$$

reduces the airfoil to $\eta = 0$. Clearly, the orthogonality of the final grid depends on the height and smoothness of this bump which are functions, of the thickness distribution along the chord of the airfoil.

1.1 Fine Mesh Regions²

Finally, we introduce a stretching transformation in ξ :

$$\xi = M_1 * y_1$$

between the trailing and leading edges, and

$$\xi = M_2 * y_2$$

(M_1 and M_2 are constants) from the trailing edge to the farfield.³ y_1 and y_2 were specified as fifth and second order polynomials,

$$y_1 = a_5 \xi'^5 + a_4 \xi'^4 + \dots + a_0$$

and

$$y_2 = b_2 \xi'^2 + b_1 \xi' + b_0,$$

respectively. We merely are stipulating that for any constant increase dy_1 or dy_2 we generate a proportional number of ξ lines; therefore, the steeper the polynomial is, the higher is the number of ξ lines. By varying the constants $a_0 - a_5$ and $b_0 - b_2$ we can control the spacing between subsequent ξ lines. This is essential for designing grids with high resolution at the leading and trailing edges.

The fifth order polynomial used between the trailing and leading edges, is uniquely determined by six boundary conditions. The start and end points (location of leading and trailing edge)

²The algorithm described in this section was developed and programmed by W. Usab.

³This scheme has been applied only to ξ lines here, but is easily extensible to η lines.

determine two constants. The remaining four constants are determined by the slopes and curvatures at the end points. Thus, for example, if we specify a high slope at the leading edge and low slope at the trailing edge we will generate grid lines clustered in the nose area and sparse approaching the trailing edge.

Three conditions must be specified for the parabola. The two endpoints, farfield and trailing edge locations, account for two of these. As the third condition, we require that the spacing between the two ξ lines immediately after the T.E. equal the spacing of the two ξ lines just before the T.E..

A sample grid, the grid used by W. Usab in the calculations mentioned in the introduction, is shown in Fig. 2, below.

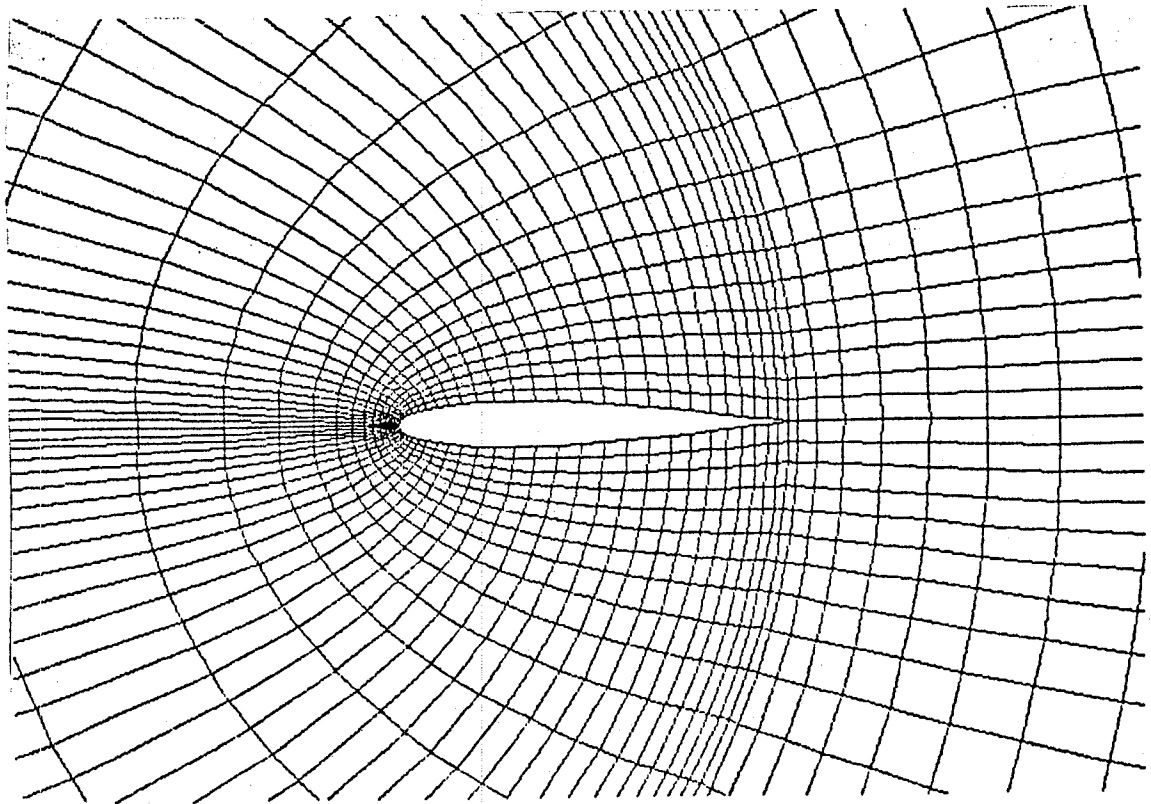


Fig. 2:
17x79 Mesh around NACA 0012 airfoil with grid line packing in
T.E. and L.E. areas.

1.2 Embedded Grids

Embedded grids are another means of achieving high resolution near critical areas. The present program is capable of embedding any number of grids (M) at a given grid level (L) at arbitrary locations. We define a level as a collection of grids with equal spacing, $\Delta\eta$ and $\Delta\xi$, in computational space.⁴

The user supplies the chordwise and normal locations of the desired embedded region in physical space, as well as the spacing at each level, which must be an integral multiple of the global spacing. The program then calculates the locations in computational space that correspond to the physical chordwise and normal locations.

The program first calculates the global mesh, saving the location of the grid nodes in computational space. Starting from the top level L , our embedding algorithm then steps through the global nodes in computational space in the positive ξ direction, comparing the value of ξ at each node to the user specified ξ_{start} and ξ_{end} . After it locates the nodes that most nearly correspond to the user specified boundaries of the first mesh M_1 at L it simply divides that embedded region into $(\xi_{end} - \xi_{start})/\Delta\xi$ node points and labels each with the appropriate value of ξ . It then does a similar search in the η direction. Having finished M_1 at L , it repeats the procedure with the other meshes $M_{2,3,\dots}$ (if any) at L and then proceeds to lower and lower levels. Some sample plots are shown in Figs. 3 & 4. Presently, the routine is being refined and adapted for use with the pointer system of W. Usab.

⁴Note, however, that $\Delta\eta = \Delta\xi$ is not required.

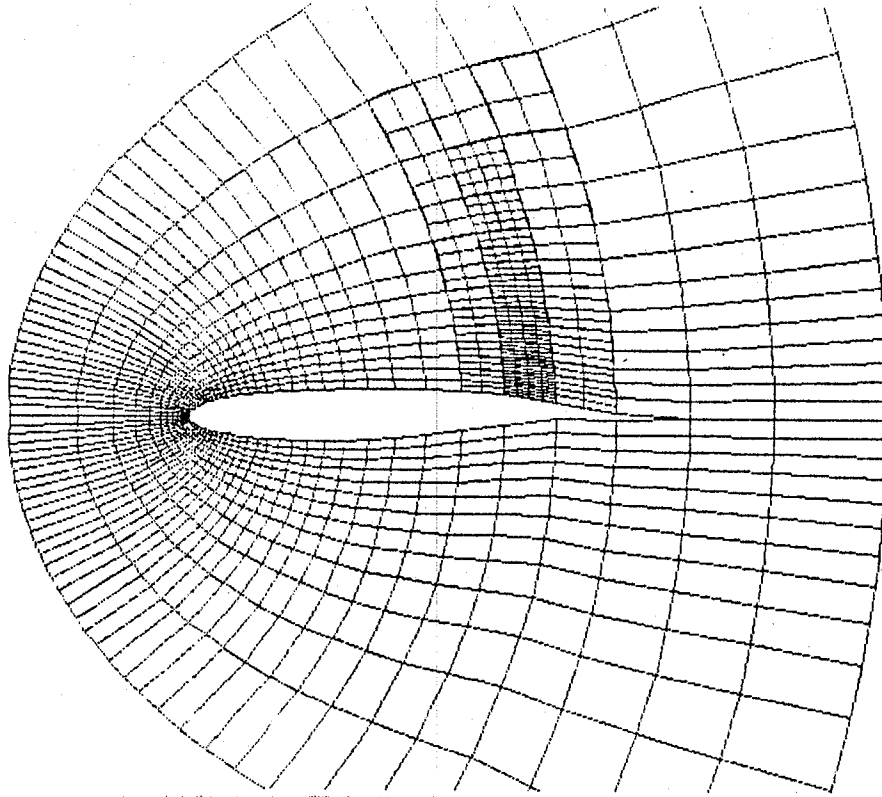


Fig. 3:
13x71 Grid with 2 levels of embedded meshes at .7 chord around
Korn & Garabedian airfoil. Level 1 has global/4 spacing (in both
 η and ξ). Level 2 has global/2 spacing.

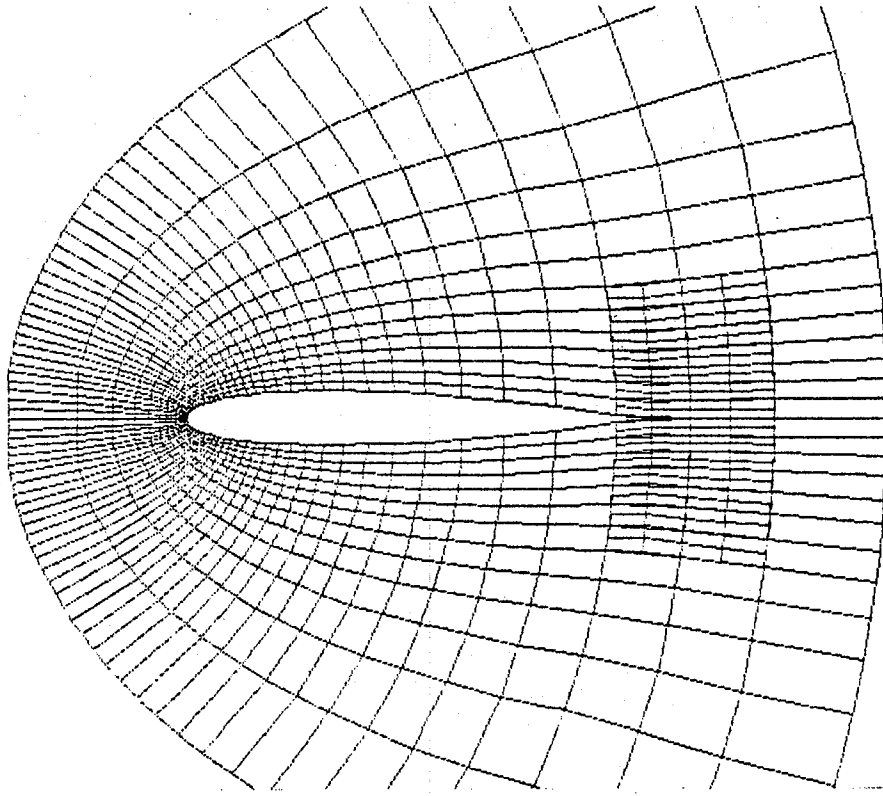


Fig. 4:
13x71 Grid with 2 embedded meshes at level 1 about NACA0012 airfoil.

2. Program Capabilities

The program generates a C-type mesh using a square root transformation coupled with a shearing transformation. For airfoil like shapes, the mesh is nearly orthogonal.

The program prompts the user for:

1. Grid outer radius (horizontal distance from mid-chord to front of grid).
2. Grid extension (distance from trailing edge to end of grid).
3. Grid spacing (in normal and tangential directions).
4. Grid line packing parameters (Note: This section is still being developed, so the operations haven't been totally "mechanized" yet.)
5. Locations of up to 10 embedded meshes per level. (Any number of levels of embedded meshes are also possible, but the highest level meshes must be input first.)

The user may also input the singular point (x_s, y_s) . A plotting subroutine provides optional plots of the mesh.

The program was written in Fortran IV and compiled and run on a VAX 750. Interactive graphics terminals were used at all stages of the grid design.

3. Program Structure

A flowchart of the computer program is given in Fig. 5, below.

C-Mesh Generator Flowchart

INPUT SECTION

Read airfoil geometry (x,y)

Solve mapping equations to go to X_1, Y_1 plane.

Fit cubic spline to airfoil in X_1, Y_1 plane.

Read boundaries of grid.
Calculate corresponding values of ξ, η with Newton routine. Read locations of fine and embedded grid areas and degree of fineness of grid.

SOLUTION ALGORITHM

Solve for ξ and η .

Interpolate with the cubic spline function to find shearing term.

Solve for X_1 and Y_1 .

Solve for x and y.

Increment ξ to ξ_{\max} .

Increment η to η_{\max} .

OUTPUT SECTION

Write and plot results.

Figure 5.

The algorithm fits a cubic spline to the first transformed coordinates of the airfoil. It is used to interpolate to find values of $Y = S(X_1)$, the shearing term. A Newton iteration routine is called whenever values of ξ and η are needed from stipulated x and y (when setting the limits of the grid, for ex.).

4. Conclusions

An algorithm for calculating C-type meshes around airfoils using the method of Jameson/Caughey is described. Generated grids are shown to be very nearly orthogonal resulting in significant improvements in flow calculations compared to previous results.

The program is very flexible. Fine mesh regions at trailing and leading edge regions may be defined conveniently. Any number of embedded grids with arbitrary spacing may be located within the global grid. Global grid characteristics such as outer radius, number of grid lines, etc., are modified easily. Several sample grids are given.

1. References

1. Wirz, H.J. and Smolderen, J.J. editors; Numerical Methods in Fluid Dynamics; 1978.
2. Jameson, A. and Caughey, D., *Numerical Calculation of the Transonic Flow Past a Swept Wing*, NY University ERDA Report; June 1977.
3. Discussion with Bill Usab; August '83.
4. Usab, W., and Murman, E. M., *Embedded Mesh Solutions of the Euler Equation Using a Multiple-grid Method*, AIAA 83-1946-CP; July 1983
5. Usab, W.; M.I.T. Dept. of Aeronautics and Astronautics, Ph.D Thesis; 1984.

End of Document